Shortwave spectral radiative signatures and their physical controls

Article

Published Version

Open access

It is advisable to refer to the publisher's version if you intend to cite from the work. See Guidance on citing.

To link to this article DOI: http://dx.doi.org/10.1175/JCLI-D-18-0815.1

www.reading.ac.uk/centaur

CentAUR

Central Archive at the University of Reading

Reading's research outputs online

Shortwave Spectral Radiative Signatures and Their Physical Controls

JAKE J. GRISTEY

Cooperative Institute for Research in Environmental Sciences, University of Colorado, and Chemical Sciences Division, NOAA/Earth System Research Laboratory, Boulder, Colorado

J. CHRISTINE CHIU

Department of Atmospheric Science, Colorado State University, Fort Collins, Colorado, and Department of Meteorology, University of Reading, Reading, United Kingdom

ROBERT J. GURNEY AND KEITH P. SHINE

Department of Meteorology, University of Reading, Reading, United Kingdom

STEPHAN HAVEMANN AND JEAN-CLAUDE THELEN

Met Office, Exeter, United Kingdom

PETER G. HILL

Department of Meteorology, University of Reading, Reading, United Kingdom

(Manuscript received 29 November 2018, in final form 2 May 2019)

ABSTRACT

The spectrum of reflected solar radiation emerging at the top of the atmosphere is rich with Earth system information. To identify spectral signatures in the reflected solar radiation and directly relate them to the underlying physical properties controlling their structure, over 90 000 solar reflectance spectra are computed over West Africa in 2010 using a fast radiation code employing the spectral characteristics of the Scanning Imaging Absorption Spectrometer for Atmospheric Chartography (SCIAMACHY). Cluster analysis applied to the computed spectra reveals spectral signatures related to distinct surface properties, and cloud regimes distinguished by their spectral shortwave cloud radiative effect (SWCRE). The cloud regimes exhibit a diverse variety of mean broadband SWCREs, and offer an alternative approach to define cloud type for SWCRE applications that does not require any prior assumptions. The direct link between spectral signatures and distinct physical properties extracted from clustering remains robust between spatial scales of 1, 20, and 240 km, and presents an excellent opportunity to understand the underlying properties controlling real spectral reflectance observations. Observed SCIAMACHY spectra are assigned to the calculated spectral clusters, showing that cloud regimes are most frequent during the active West African monsoon season of June–October in 2010, and all cloud regimes have a higher frequency of occurrence during the active monsoon season of 2003 compared with the inactive monsoon season of 2004. Overall, the distinct underlying physical properties controlling spectral signatures show great promise for monitoring evolution of the Earth system directly from solar spectral reflectance observations.

Corresponding author: Jake J. Gristey, jake.j.gristey@noaa.gov

1. Introduction

Knowledge of the total reflected solar radiation (RSR) by Earth is vital for quantification of the global energy budget, and therefore essential for monitoring,

predicting and understanding how climate is evolving (Stephens et al. 2015). As a result, broadband (i.e., spectrally integrated) RSR has been observed from satellites by dedicated energy budget missions for decades (Vonder Haar and Suomi 1971; Barkstrom 1984; Kyle et al. 1993; Wielicki et al. 1996; Harries et al. 2005). These observations have had many uses, including quantifying fundamental climate parameters such as the planetary brightness (Vonder Haar and Suomi 1971), understanding climate forcing and feedbacks (Futyan et al. 2005; Loeb et al. 2007; Brindley and Russell 2009; Dessler 2013; Ansell et al. 2014), and evaluating and improving climate models (Forster and Gregory 2006; Tett et al. 2013a,b; Hartmann and Ceppi 2014).

Although the RSR has most commonly been observed and applied in its broadband form, it is fundamentally an intricate spectral quantity. Such intricacy results from wavelength specific interactions between the incoming solar radiation and atmospheric gases, aerosols, clouds, and the surface. Since it is often precisely these atmospheric and surface properties that we seek to understand from RSR measurements, the spectral dimension contains a vast amount of relevant information (Feldman et al. 2011; Coddington et al. 2012; King and Vaughan 2012). This also applies to the longwave spectrum, where the spectral variability has been widely investigated (e.g., Harries et al. 1998; Huang and Yung 2005; Huang et al. 2014) and applied to evaluate model forcing and feedbacks (Huang et al. 2007, 2010; Leroy et al. 2008). In contrast, observation and application of the RSR spectrum for identifying underlying properties and processes of the Earth system is less well developed (Brindley and Bantges 2016).

Perhaps the most notable investigations of the RSR spectrum have utilized observations from the Scanning Imaging Absorption Spectrometer for Atmospheric Chartography (SCIAMACHY), which will be fully introduced in section 2a. For example, SCIAMACHY observations have helped to explain the observed symmetry in hemispheric albedo, which has long been known (Ramanathan 1987) and has been investigated further in recent years (Voigt et al. 2013, 2014, Stephens et al. 2015, 2016; Haywood et al. 2016). Essentially, the hemispherical spectral albedo from the SCIAMACHY reveals that near-infrared reflection from a higher fraction of relatively bright landmass in the Northern Hemisphere is balanced by visible reflection from a higher fraction of relatively bright clouds in the Southern Hemisphere (Stephens et al. 2015), a signal that is completely masked in the equivalent broadband observations. Other pioneering work has revealed the dominant spectral contributions to the variance in SCIAMACHY observations (Roberts et al. 2011) that are expected to be related to certain properties of the Earth system. While it was not possible to know the precise physical properties controlling each spectral contribution by analyzing SCIAMACHY observations alone, Roberts et al. (2011) discussed likely general causes such as cloud and various surface types. Subsequent work has provided further understanding via detailed comparisons with the spectral variability simulated using climate model output (Roberts et al. 2013, 2014). However, a direct link between observed RSR spectra and the underlying Earth system properties controlling their structure remains elusive.

This study aims to quantitatively relate RSR spectral signatures to specific surface and atmospheric properties, examine how this relationship changes with spatial scale, and provide a route forward for monitoring these properties directly from spectrally resolved observations. Central to achieving this aim is the extraction of spectral signatures via clustering of RSR spectra that are computed using atmospheric and surface properties derived from A-Train satellite observations. Using this technique, the exact properties controlling the RSR spectra are known and not subject to climate model biases. Clustering has been widely used in atmospheric science, for example to identify clusters of CloudSat reflectivity profiles in the tropics (Zhang et al. 2007; Young 2015) and to identify "weather states" using joint histograms of cloud-top height and optical depth (Jakob and Tselioudis 2003; Williams and Tselioudis 2007; Williams and Webb 2009; Oreopoulos et al. 2014), but has not been directly applied to reflectance spectra. This unique approach provides the opportunity to examine cloud regimes emerging solely from spectral radiative effects, providing new insights at scales relevant to various satellite observation, numerical weather prediction, and climate modeling communities.

The satellite datasets and radiative transfer tools used to compute RSR spectra are described alongside the method of extracting spectral signatures in section 2. Spectral signatures are presented in section 3, and the underlying atmospheric and surface properties associated with each signature are examined in detail at different spatial scales. Importantly, section 3 highlights the key role of the spectral shortwave cloud radiative effect (SWCRE) in identifying cloud regimes that are markedly different to existing classifications, and the potential for monitoring the relative frequency of these signatures in real SCIAMACHY observations. A brief summary is provided in section 4.

2. Data and methodology

a. Observed hyperspectral reflectance from SCIAMACHY

SCIAMACHY was a hyperspectral imaging spectrometer aboard the sun-synchronous *Environmental Satellite* (*Envisat*) from 2002 to 2012, crossing the equator

at 1000 local time. It measured the incoming and reflected solar spectrum between wavelengths of 0.214–2.386 μm, with spectral resolution between 0.00022 and 0.00148 μm depending on the spectral region (Gottwald and Bovensmann 2011). SCIAMACHY's primary objective was to perform global measurements for trace gas retrieval, but the measurements have also been used to retrieve cloud and aerosol properties (Kokhanovsky et al. 2005; von Hoyningen-Huene et al. 2007). The narrow spectral bands used for trace gas retrieval are available with relatively short measurement integration times, leading to spatial resolution of around 26 km × 30 km. However, the full spectrum is only available with longer integration times, giving a nadir footprint of around 30 km × 240 km.

We extract SCIAMACHY nadir spectral reflectance observations (version 8) and use them to monitor the frequency of spectral signatures and their controlling properties as identified from radiative transfer computations (see section 2b). SCIAMACHY spectral reflectance $R_{\lambda,\text{SCIA}}$ is calculated within the SCIAMACHY product as

$$R_{\lambda,\text{SCIA}} = \frac{\pi I_{\lambda,\text{SCIA}}}{S_{\lambda,\text{SCIA}} \cos(\theta)}, \tag{1}$$

where π has units of steradians (sr); $I_{\lambda,\text{SCIA}}$ is the observed SCIAMACHY outgoing spectral radiance (W m^{-2} sr^{-1}); $S_{\lambda,\text{SCIA}}$ is the observed SCIAMACHY incoming spectral irradiance that is updated daily (W m^{-2}); θ is the solar zenith angle; and an assumption of isotropic radiation has been made. The radiation variables are all a function of wavelength λ.

Several exclusions and modifications are applied. First, we focus on the spectral range from 0.250 to 1.750 μm because the spectrum beyond 1.750 μm suffered from unreliable optical throughput due to ice deposits on the detectors (Gottwald and Bovensmann 2011). Second, spurious signal is filtered out by removing reflectance associated with large differences (>20%) at neighboring wavelengths. This threshold effectively removes the spurious signal while retaining the sharpest real spectral variability at the SCIAMACHY native spectral resolution. Finally, the SCIAMACHY spectral reflectance is gridded to a consistent 0.001-μm spectral resolution. This has been shown to be ample resolution to retain the variance contributions from the dominant components of spectral variability (Roberts et al. 2011).

b. Computed hyperspectral reflectance

1) INPUT FROM A-TRAIN SATELLITE OBSERVATIONS

To improve understanding of the physical controls on spectral RSR variability, radiative transfer computations

are performed using input from A-Train satellite observations. Specifically, we use release B1 of the CERES–*CALIPSO*–*CloudSat*–MODIS (CCCM) product (Kato et al. 2010, 2011), which collocates irradiance derived from the Clouds and the Earth's Radiant Energy System (CERES) with cloud, aerosol, and surface properties retrieved from the *Cloud–Aerosol Lidar and Infrared Pathfinder Satellite Observations* (*CALIPSO*) Cloud–Aerosol Lidar with Orthogonal Polarization (CALIOP), the *CloudSat* Cloud Profiling Radar (CPR), and the Moderate Resolution Imaging Spectroradiometer (MODIS). The product was designed to provide detailed cloud and aerosol profiles that are consistent with the observed radiative fluxes and thus is well suited for process studies.

Among these sensors, the CERES has the largest footprint size of ~20 km. Within each CERES footprint, up to 16 groups (henceforth referred to as "CCCM groups") containing either clear-sky or different vertical profiles of cloud are determined, based on their cloud boundaries [see Kato et al. (2010) for details]. For each CCCM group that contains cloud, the mean cloud properties from the CPR, CALIOP, and MODIS at a spatial resolution of 1 km are combined, using the method described in Bodas-Salcedo et al. (2016), resulting in profiles of liquid/ice water content and effective radii at a vertical resolution of ~240 m. Other than the cloud profiles, all properties are horizontally uniform across the CERES footprint. These properties include vertical profiles of aerosol extinction from CALIOP and MODIS, vertical profiles of atmospheric temperature, water vapor and ozone that are added to the CCCM dataset from the Goddard Earth Observing System Model (GEOS) reanalysis, and surface spectral reflectance over land from MODIS. Over ocean, where surface reflectance is not provided, we use a default spectrally flat surface reflectance of 0.2; while this value can range from approximately 0.02 to 0.4 depending on solar zenith angle and wind speed (Li et al. 2006), our default value is larger than most estimates. It is therefore more demanding for our clustering technique to distinguish clear-sky scenes over the ocean from other scenes; despite this, we will show that clear-sky ocean scenes are very effectively identified, and this would have been even more effective had a lower value been used. The exact value of ocean surface albedo used is not expected to change our conclusions.

To understand radiative signatures under a variety of surface, atmospheric, and cloud conditions, we extracted CCCM data for all seasons in 2010, and for the region bounded by 20°W–20°E and 0°–30°N, henceforth referred to as "West Africa." This results in 90 917 CCCM groups. The year of 2010 was chosen because the West

African monsoon was particularly active during this year (as we will show later in Fig. 14a), providing the possibility to extract a diverse range of atmospheric signatures across West Africa. West Africa was chosen because it has attracted substantial interest in recent years due to complex atmospheric physics, poor climate model performance, and a growing population (Knippertz et al. 2015; Hill et al. 2016, 2018; Hannak et al. 2017). The diverse surface types (from dark ocean, to vegetated surface, to bright desert) and diverse cloud systems (from marine boundary layer clouds, to multilayer clouds, to deep convective clouds; Stein et al. 2011) also provide variety to ensure the representativeness of our spectral signature extraction. Snow cover is one important physical property not represented in this region. It is expected that the dataset described by Bodas-Salcedo et al. (2016) and used by Hill et al. (2018) will be extended globally in the future to address this issue.

2) FAST RADIATIVE TRANSFER

Using the detailed scene properties provided by CCCM as input, corresponding top-of-atmosphere reflectance spectra are computed using the Havemann–Taylor Fast Radiative Transfer Code (HT-FRTC) (Havemann et al. 2018). The HT-FRTC is a 1D radiative transfer code that relies on a principal component approach to expedite hyperspectral computations, and can be applied to the spectral regions from ultraviolet to microwave. Relative to line-by-line calculations, the principal component approach is capable of producing spectral reflectance to an accuracy well within 0.01, and mostly to within 0.005 (see Fig. 6 in Havemann et al. 2018). Profiles of water vapor, carbon dioxide, ozone, and methane are input to the code, while standard concentrations of more minor absorbing species are prespecified. Gaseous absorption coefficients are derived from line-by-line calculations as described in Havemann et al. (2018).

Hyperspectral radiance was computed at substantially higher spectral resolution than that of SCIAMACHY and was then averaged over the SCIAMACHY spectral response functions to obtain a radiance spectrum consistent with SCIAMACHY spectral sampling (henceforth referred to as "SCIAMACHY-like"). For a given CCCM group, a SCIAMACHY-like reflectance spectrum $R_{\lambda,\text{CCCM}-1\text{km}}$, is given by

$$R_{\lambda,\text{CCCM}-1\text{km}} = \frac{\pi I_{\lambda,\text{CCCM}-1\text{km}}}{s^* S_{\lambda,0} \cos(\theta)}, \qquad (2)$$

where $I_{\lambda,\text{CCCM}-1\text{km}}$ is the computed SCIAMACHY-like nadir outgoing radiance spectrum at the top-of-atmosphere; s^* is a factor that accounts for variations

in the Earth–sun distance; and $S_{\lambda,0}$ is the incoming solar irradiance spectrum at the mean Earth–sun distance from Kurucz and Bell (1995) averaged over the SCIAMACHY spectral response functions. The solar zenith angle θ is calculated to be consistent with the date, time, and location of the CCCM observation. As in Eq. (1), an isotropic assumption is made, and for consistency with the SCIAMACHY observations (section 2a), the radiation variables are gridded at a 0.001-μm spectral resolution for wavelengths from 0.250 to 1.750 μm.

Since the set of $R_{\lambda,\text{CCCM}-1\text{km}}$ spectra are based on cloud profiles at the finest spatial resolution, we discuss their characteristics and associated controlling factors in detail in section 3a. However, as mentioned earlier, SCIAMACHY has a much coarser horizontal resolution of ~240 km in the cross-track direction, and thus averaging of computed spectra is required to better match SCIAMACHY observations. We first calculate the mean reflectance for each CERES ~20-km footprint $R_{\lambda,\text{CCCM}-20\text{km}}$ by summing up the computations for individual CCCM groups weighted by their fraction F, that is,

$$R_{\lambda,\text{CCCM}-20\text{km}} = \sum_{i=1}^{M} F_i \times R_{\lambda,\text{CCCM}-1\text{km},i}, \qquad (3)$$

where i and M represent the index of the CCCM group and the total number of CCCM groups in the CERES footprint, respectively. By averaging $R_{\lambda,\text{CCCM}-20\text{km}}$ over 12 consecutive CERES footprints that form a long strip of around 240 km, the mean $R_{\lambda,\text{CCCM}-240\text{km}}$ represents spectra at a similar spatial resolution to SCIAMACHY and is given by

$$R_{\lambda,\text{CCCM}-240\text{km}} = \frac{\sum_{j=1}^{12} R_{\lambda,\text{CCCM}-20\text{km},j}}{12}, \qquad (4)$$

where j is the CERES footprint index. Equation (4) implies that only cases where 12 consecutive CERES footprints are available are included, which is sometimes not possible if the edge of the domain is reached, or if all observations within one of the CERES footprints fail basic quality checks (e.g., if the observed cloud profiles and reanalyzed temperature profiles result in liquid cloud at temperatures below 233 K or ice cloud at temperatures above 273 K). As a result, the $R_{\lambda,\text{CCCM}-240\text{km}}$ values do not incorporate all $R_{\lambda,\text{CCCM}-20\text{km}}$, but the entire West Africa domain remains well represented so we do not expect this to impact our conclusions. Since Eqs. (3) and (4) introduce inhomogeneity in the along-track direction only, homogeneity remains in the cross-track direction, where the cloud information remains at a

smaller scale than the width of the SCIAMACHY footprint.

Finally, to quantify the spectral SWCRE of computed spectra, the process from Eqs. (2)–(4) is repeated with cloud removed from the input profiles. At each spatial scale, the spectral SWCRE, in reflectance units, is simply calculated as the difference between the SCIAMACHY-like reflectance computed with and without cloud. This is the standard and recommended method for computing SWCRE in models (Cess and Potter 1987; Potter et al. 1992), although it can be biased relative to observations. We also present the broadband (i.e., integral over 0.250–1.750 μm) SWCRE (in units of W m^{-2}) at the satellite overpass time, calculated as the difference between the SCIAMACHY-like radiance computed with and without the cloud, using an isotropic assumption to convert the radiance difference to a flux difference.

While CCCM provides information on seven common aerosol species, only four of them (large dust particles, small dust particles, sulfate, and sea salt) are used, since their optical properties have been included in the training phase of HT-FRTC. These four types account for over 85% of the total aerosol fraction in the study region and time period considered such that aerosol variability is expected to be reasonably well represented. Training of the HT-FTRC for other aerosol types, including more strongly absorbing types that may be of particular significance in the study region, is currently being investigated and will allow inclusion of more aerosol types in the future.

c. Radiative signature clustering and monitoring

To identify distinct spectral signatures, we performed k-means clustering analysis (Anderberg 1973) for SCIAMACHY-like reflectance spectra across the various spatial scales (i.e., $R_{\lambda,\text{CCCM–1km}}$, $R_{\lambda,\text{CCCM–20km}}$, and $R_{\lambda,\text{CCCM–240km}}$). To avoid confusion among spatial scales, clusters are identified with lowercase letters for $R_{\lambda,\text{CCCM–1km}}$ (e.g., cluster a, b, etc.), roman numerals for $R_{\lambda,\text{CCCM–20km}}$ (e.g., cluster I, II, etc.), and numbers for $R_{\lambda,\text{CCCM–240km}}$ (cluster 1, 2, etc.). The clustering procedure works by starting with a predefined number of random spectra from the full dataset, calculating the mean of the individual spectra that are closest to each of these starting spectra, and iterating until convergence. The final set of mean spectra are referred to as cluster centroids. Once cluster centroids are identified, we analyzed the input surface and atmospheric properties used to compute the SCIAMACHY-like reflectance spectra belonging to each cluster.

Using the resulting clusters derived from SCIAMACHY-like reflectance spectra at a spatial scale similar to the

SCIAMACHY footprint (i.e., $R_{\lambda,\text{CCCM–240km}}$), we then use actual observations from SCIAMACHY to gain insight into the controlling properties of spectral reflectance. Specifically, each SCIAMACHY observed spectrum is assigned to a particular cluster for which the root-mean-square difference (RMSD) between the SCIAMACHY observation and the simulated cluster centroid suggested by $R_{\lambda,\text{CCCM–240km}}$ is smallest. The RMSD is defined as

$$\text{RMSD} = \sqrt{\frac{\sum_{\lambda=\lambda_1}^{\lambda_N}(R_{\lambda,\text{SCIA}} - R_{\lambda,\text{CCCM–240km,centroid}})^2}{N}}, \quad (5)$$

where $R_{\lambda,\text{CCCM–240km,centroid}}$ is a given centroid from the cluster analysis of $R_{\lambda,\text{CCCM–240km}}$; N is the total number of wavelengths; and $\{\lambda_1, \lambda_N\}$ are the first and last wavelengths of 250 and 1.750 μm, respectively.

3. Results

a. Clusters of computed reflectance spectra

1) SPECTRAL SIGNATURES AND THEIR CONTROLLING PROPERTIES

Clustering of more than 90 000 computed SCIAMACHY-like reflectance spectra for individual CCCM groups over West Africa in 2010 leads to the 10 centroids shown in Fig. 1. The standard deviation of computed spectra belonging to each cluster is relatively small (Fig. 2), indicating that the centroids represent the spectra in each cluster well. The spread of reflectance in gaseous absorption bands is relatively small for all clusters, but in atmospheric windows it is more variable between clusters, showing that the spread of reflectance due to variability in the properties controlling each cluster can be different. The choice of 10 clusters works appropriately to separate surface, liquid cloud, and ice cloud signatures. For all clusters, gaseous absorption is evident; for example, the relatively broad water vapor absorption bands around 0.93, 1.13, and 1.39 μm, and sharp oxygen A and B absorption bands centered at 0.762 and 0.688 μm, respectively. The cluster analysis not only captures the differences in the magnitude of the spectrum (e.g., the "darker" spectrum in cluster d versus the "brighter" spectrum in cluster h), but also the shape (e.g., the relatively flat spectrum in cluster c versus the much more variable spectrum in cluster e).

The clusters fall into two broad categories: those dominated by surface reflectance (henceforth "surface clusters") and those dominated by cloud reflectance (henceforth "cloud clusters"); see Table 1. The surface
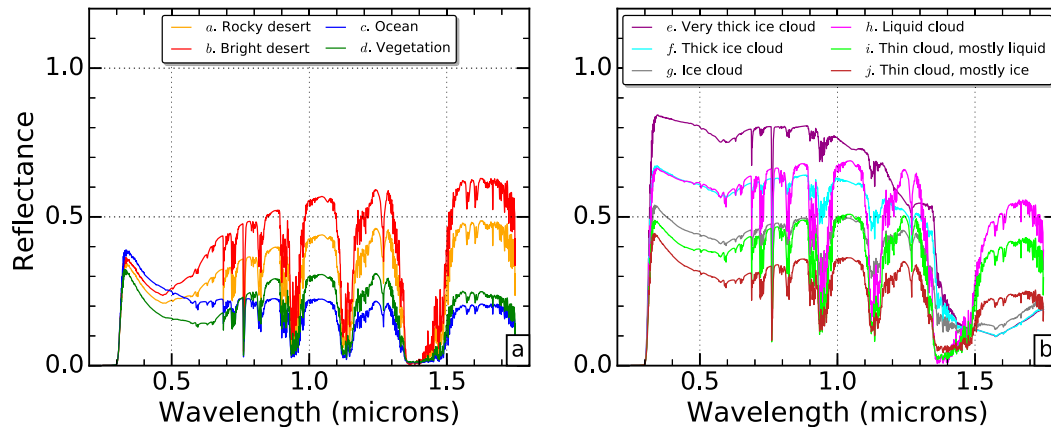
FIG. 1. Cluster centroids of top-of-atmosphere reflectance spectra at a spatial scale of 1 km. Ten clusters are shown, separated into (a) surface clusters and (b) cloud clusters; further details are provided in Table 1. The cluster centroids are identified from 90 917 computed SCIAMACHY-like reflectance spectra that are regridded to a 0.001-μm spectral resolution. Input for the computations is derived from A-Train satellite observations over West Africa in 2010. Computations are performed using the Havemann–Taylor Fast Radiative Transfer Code.

clusters (clusters a–d; Fig. 1a) are characterized by spectra with relatively small spread in the input surface reflectance (Figs. 3a–d), are highly constrained to locations with certain surface types (Figs. 4a–d), and have very little cloud liquid or ice in the mean input profiles (Figs. 5a–d). Cluster a has the largest sample size (Table 1), representing signatures mainly associated with rocky desert surface reflectance that increases from around 0.2 in the visible to 0.5 in the near-infrared (Fig. 3a). As shown in Fig. 4a, spectra from cluster a predominantly originate from outskirts and rocky hamada of the Sahara desert (i.e., elevated stone plateaus where most of the sand has been removed by deflation), with notable gaps over brighter surfaces containing sand dunes. Data points over these sand dunes are captured by cluster b (Fig. 4b), which has a surface reflectance spectrum similar to cluster a, but with larger magnitude (Fig. 3b). Clusters c and d represent signatures from darker ocean and vegetated surfaces, respectively, as confirmed by Figs. 4c and 4d. Unsurprisingly, the ocean surface represented by cluster c has a spectrally flat surface reflectance value of 0.2 (Fig. 3c), as this is the default value used for ocean surfaces [see section 2b(1)]. The vegetated surface represented by cluster d exhibits a sudden jump in surface reflectance around 0.67 μm (Fig. 3d), commonly referred to as the ''red edge.'' Overall, all of these surface clusters have mean vertically integrated cloud water content less than $10 \, \mathrm{g \, m^{-2}}$ (Figs. 5a–d), allowing the underlying surface to be the primary factor that controls the top-of-atmosphere reflectance spectra.

Cloud clusters (clusters e–j; Fig. 1b) all contain a substantial amount of cloud water on average (Figs. 5e–j)

and can be less well constrained by location (Figs. 4e–j) and therefore typically exhibit large spread in spectral surface reflectance (Figs. 3e–j). Starting with the centroids of clusters e, f, and g, which are associated with relatively large reflectance up until 1.3 μm but with different spectral shapes between 1.3 and 1.7 μm compared to other centroids (Fig. 1b), since ice absorption is much stronger than liquid absorption around 1.6 μm and much weaker around 1.4 μm (Pilewskie and Twomey 1987), the reduced reflectance around 1.6 μm and increased reflectance around 1.4 μm for these centroids indicates the presence of ice clouds. This is confirmed by their average cloud profiles (Figs. 5e–g), revealing predominantly ice cloud that peaks in ice water content at around 11-km altitude.

Compared to clusters e–g that are dominated by ice clouds, the centroid of cluster h has similar magnitudes of reflectance up until 1.3 μm, but lower around 1.4 μm and higher around 1.6 μm (Fig. 1b). The generally large reflectance throughout the spectrum and opposite spectral signature to ice cloud between 1.3 and 1.7 μm indicates the presence of liquid cloud and the absence of ice cloud, as confirmed by Fig. 5h. The centroids of clusters i and j have similar spectral shapes to cluster h, but with smaller magnitudes (Fig. 1b). The smaller magnitudes indicate that clouds are, on average, optically thinner in these two clusters than cluster h. Therefore, surface influence cannot be ignored, as evidenced by the location of the spectra in cluster j (Fig. 4j), which avoid the brightest desert surfaces.

Figure 6 shows that the aerosol loadings are similar between clusters, suggesting that no particular cluster is dominated by aerosol–radiation interactions. The mean
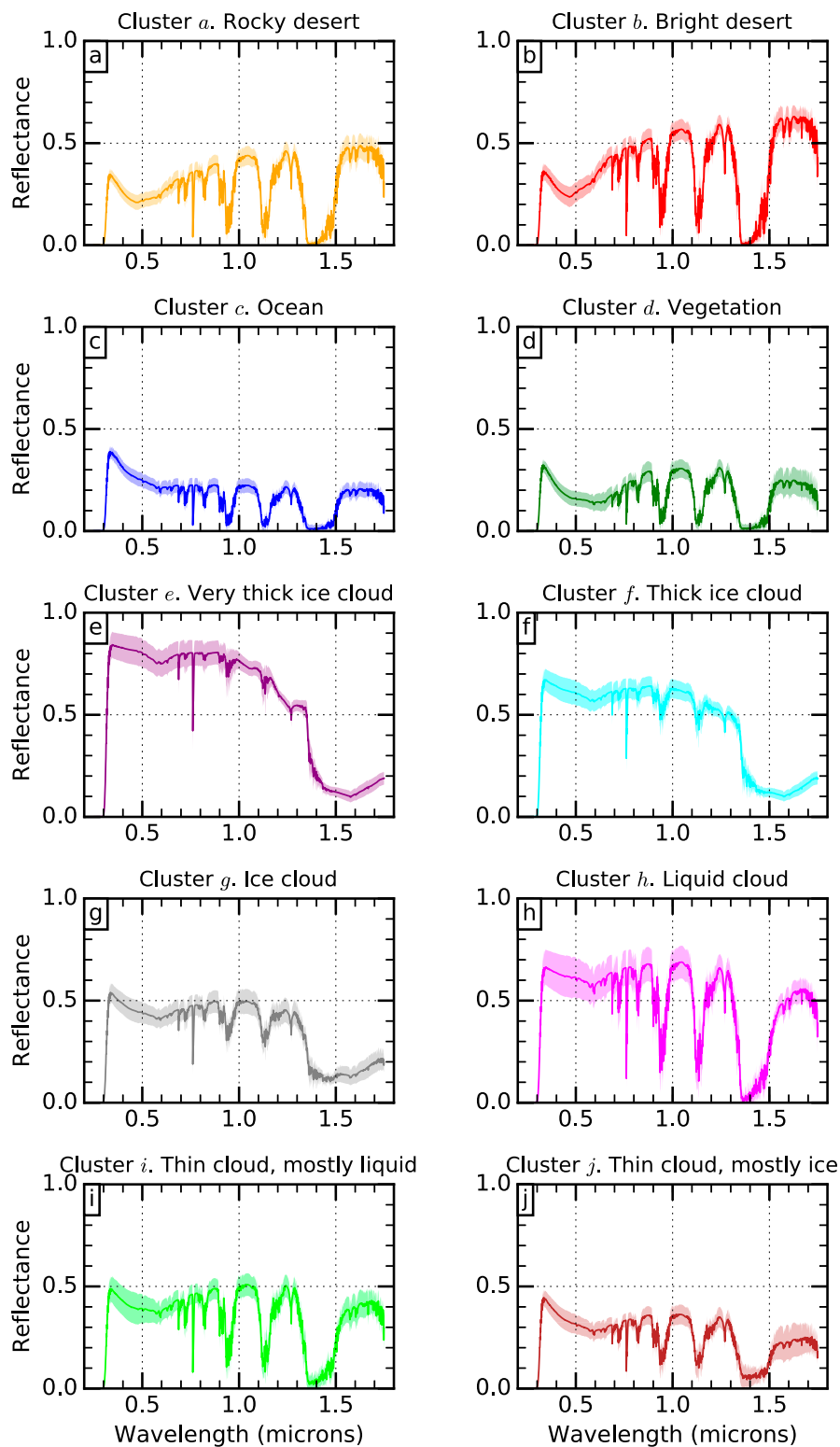
FIG. 2. The 10 cluster centroids presented in Fig. 1, but each plotted separately. The shaded regions represent one standard deviation either side of the cluster centroid for individual spectra that fall into each cluster.

TABLE 1. Summary of the 10 clusters presented in Fig. 1 and their dominating properties, based on 90 917 computed SCIAMACHY-like reflectance spectra over West Africa in 2010.

Cluster identifier	Assigned color	Comment on controlling property	Designated as surface or cloud dominated?	No. of spectra
a	Orange	Rocky desert	Surface	12 408
b	Red	Bright desert (sand dunes)	Surface	11 882
c	Blue	Ocean	Surface	10 816
d	Green	Vegetation	Surface	9258
e	Purple	Very optically thick ice cloud	Cloud	5872
f	Cyan	Optically thick ice cloud	Cloud	8267
g	Gray	Ice cloud	Cloud	9045
h	Magenta	Liquid cloud	Cloud	3354
i	Lime	Vertically distributed but optically thin cloud, mostly liquid	Cloud	8487
j	Brown	Vertically distributed but optically thin cloud, mostly ice, over dark surface	Cloud	11 528

column integrated aerosol for each cluster, as shown in the top right of each panel in Fig. 6, is within one standard deviation either side of the mean for any other cluster. Some notable differences in aerosol profiles do exist between surface clusters that appear to be a by-product of the location of the spectra. For example, the highest mean percentage of sea salt is found in cluster c, but this is because cluster c is predominantly controlled by ocean surface reflectance. The absence of aerosol signature in our clusters is perhaps surprising given that West Africa is associated with diverse aerosol types and loadings (Knippertz et al. 2015). However, recall that only a subset of the aerosol types are included in the computations [see section 2b(2)] and of the aerosol types considered here, the variety is dominated by dust, which constitutes over 90% of the mean aerosol loading for all clusters.

2) CLOUD RADIATIVE EFFECTS OF EACH CLUSTER

Cloud clusters exhibit distinct spectral SWCRE (in reflectance units) and a large range in mean broadband SWRCE (in $W m^{-2}$) as shown in Fig. 7. Surface clusters are not shown because SWCRE is low throughout the spectrum (broadband SWCRE less than $30 W m^{-2}$) due to their low average cloud water content. However, the standard deviation of broadband SWCRE for surface clusters is greater than the mean, suggesting that profiles with nonnegligible cloud amount can occasionally fall into surface clusters.

For cloud clusters, a number of key features are found. First, the mean broadband SWCREs range from 200 to over $500 W m^{-2}$ for clusters with relatively optically thick clouds (clusters e, f, g, and h) and between 110 and $170 W m^{-2}$ for clusters with relatively optically thin clouds (clusters i and j). The stated values of broadband

SWCRE are instantaneous at the time of satellite overpass; the annual cycle of solar zenith angle will therefore lead to some variations in the amount of incoming solar radiation, but the sun-synchronous orbit of the A-Train satellites with an equator crossing of around 1330 local time provides diurnal consistency over the West Africa region considered.

The second key feature is the swing from positive to negative spectral SWCRE around $1.5 \mu m$ for clusters associated with ice cloud (clusters e, f, and g). The presence of the swing is a good example of the added value from monitoring SWCRE spectrally; in an equivalent broadband measurement, the positive and negative SWCRE from different parts of the spectrum partly compensate. This can make the broadband SWCRE from two distinctly different cloud regimes appear quite similar (e.g., the mean broadband SWCRE for clusters g and i, respectively associated with ice cloud and vertically distributed thin liquid cloud, are within $40 W m^{-2}$), despite relatively large spectral differences.

Finally, the spectral SWCRE in water vapor absorption bands (e.g., around 0.93, 1.13, and $1.39 \mu m$) have reversed directions (i.e., bump vs dip) among cloud clusters. Pronounced bumps occur when ice clouds are present (most notably clusters e, f, and g). Ice clouds reflect solar radiation back to space at high altitudes before it can interact with the large water vapor concentrations in the lower troposphere. Therefore, the reflectance difference in water vapor bands between cloud-free conditions, corresponding to low reflectance due to strong water vapor absorption, and cloudy conditions, corresponding to higher reflectance due to more reflection back to space at high altitudes, is larger than the difference at surrounding wavelengths. Conversely, pronounced dips occur when optically thick liquid
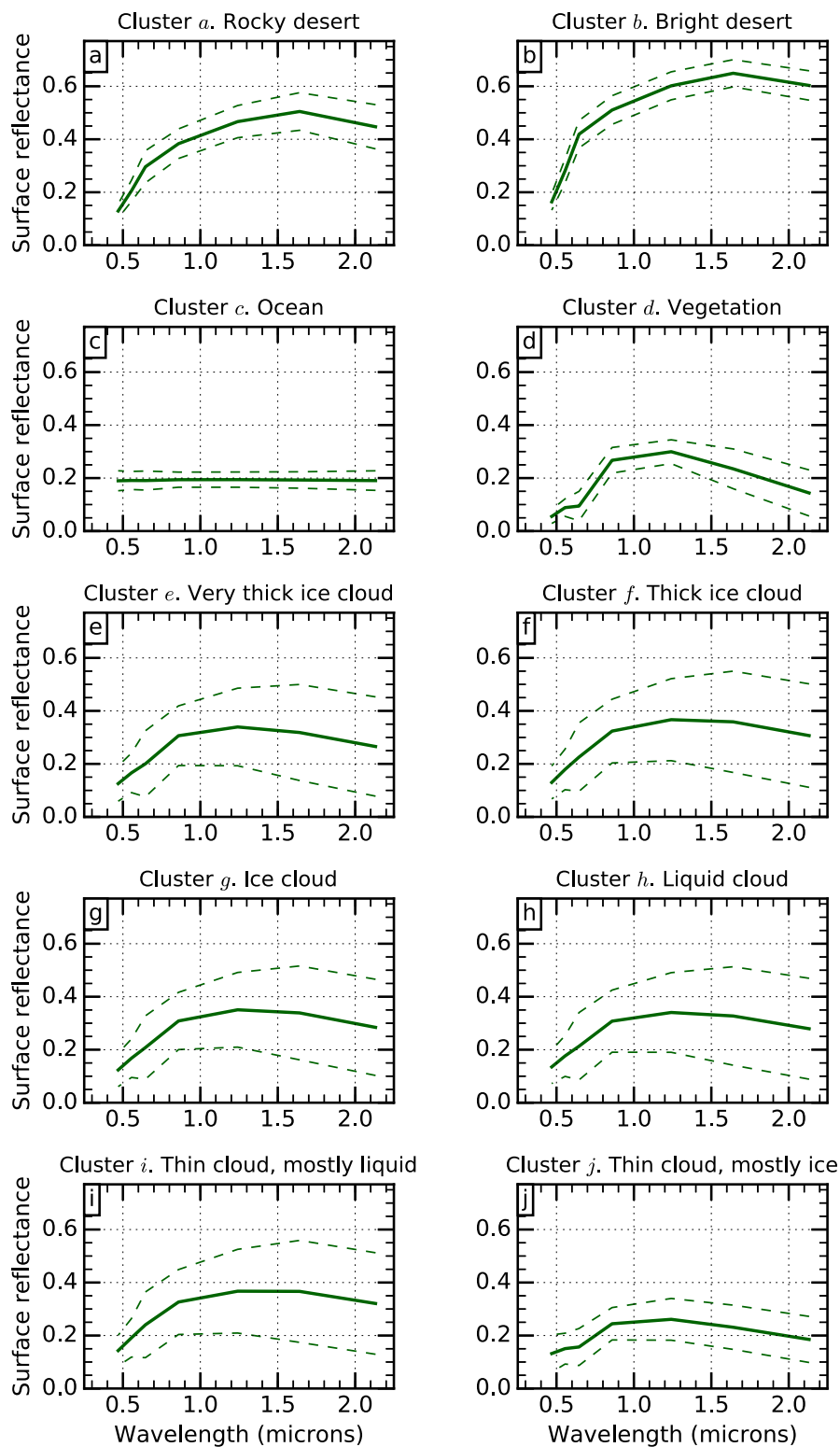
FIG. 3. The mean surface spectral reflectance used as input in computed SCIAMACHY-like reflectance spectra belonging to each of the 10 clusters presented in Fig. 1. The dashed lines represent one standard deviation either side of the mean.
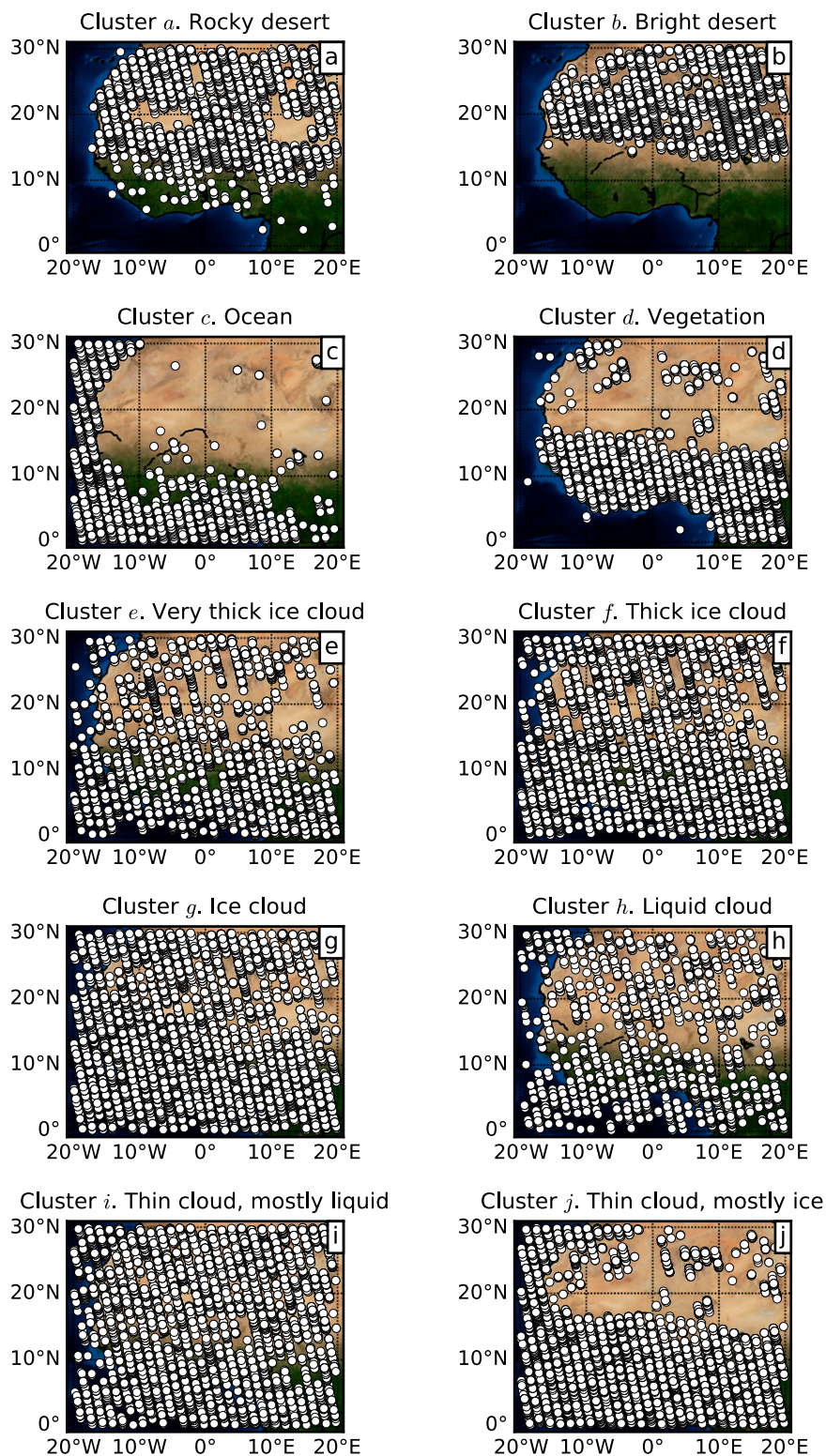
FIG. 4. The location of the computed SCIAMACHY-like reflectance spectra belonging to each of the 10 clusters presented in Fig. 1. Each location is represented by a white dot. The background map is based on the true-color "blue marble" image (Stockli et al. 2005).
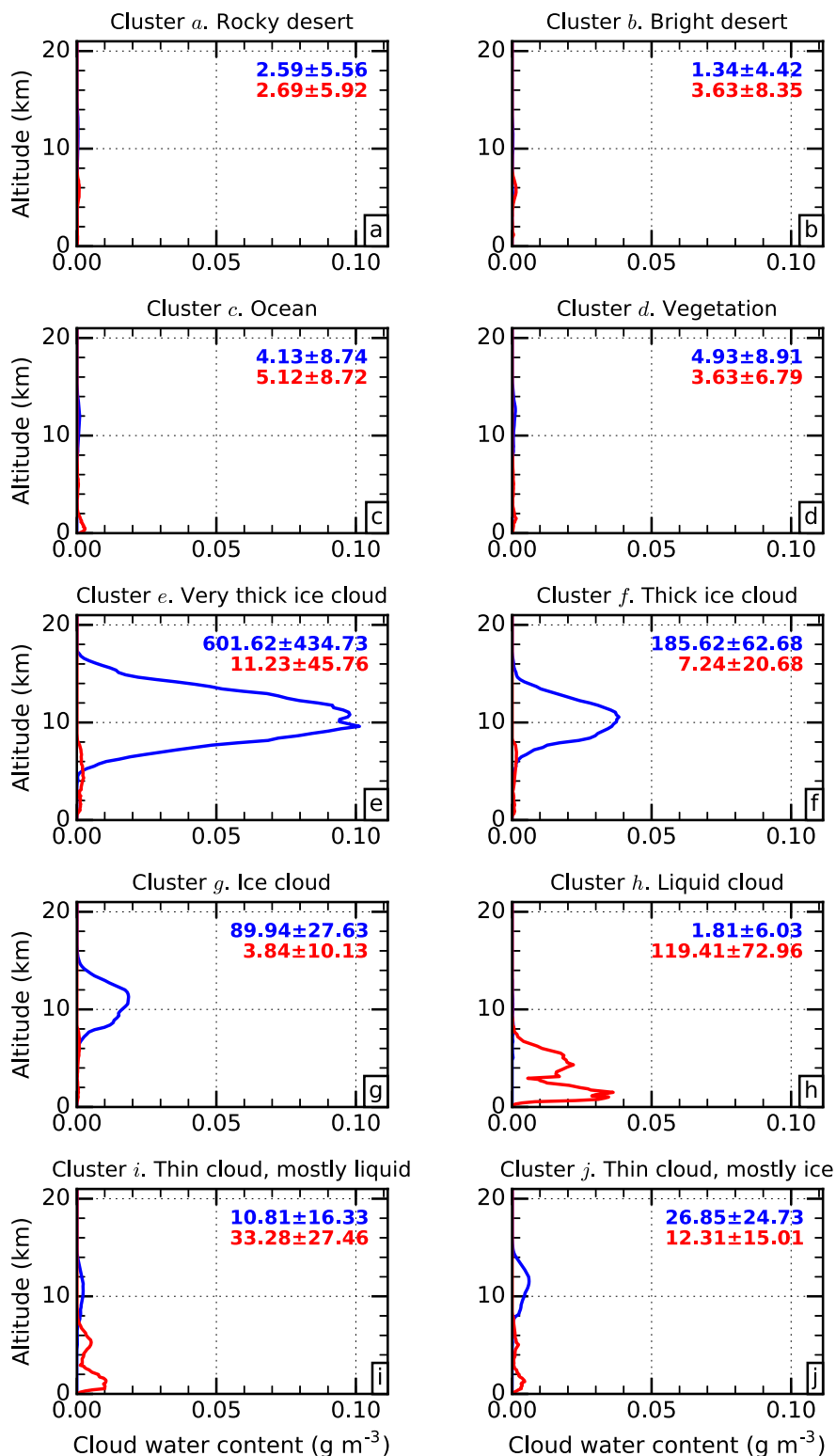
FIG. 5. The mean vertical profile of ice (blue) and liquid (red) cloud water content used as input in computed SCIAMACHY-like reflectance spectra belonging to each of the 10 clusters presented in Fig. 1. The vertically integrated ice and liquid water content for the mean cloud vertical profile of each cluster is displayed on each plot, with ± 1 standard deviation of individual vertically integrated liquid and ice water contents ($g\,m^{-2}$).
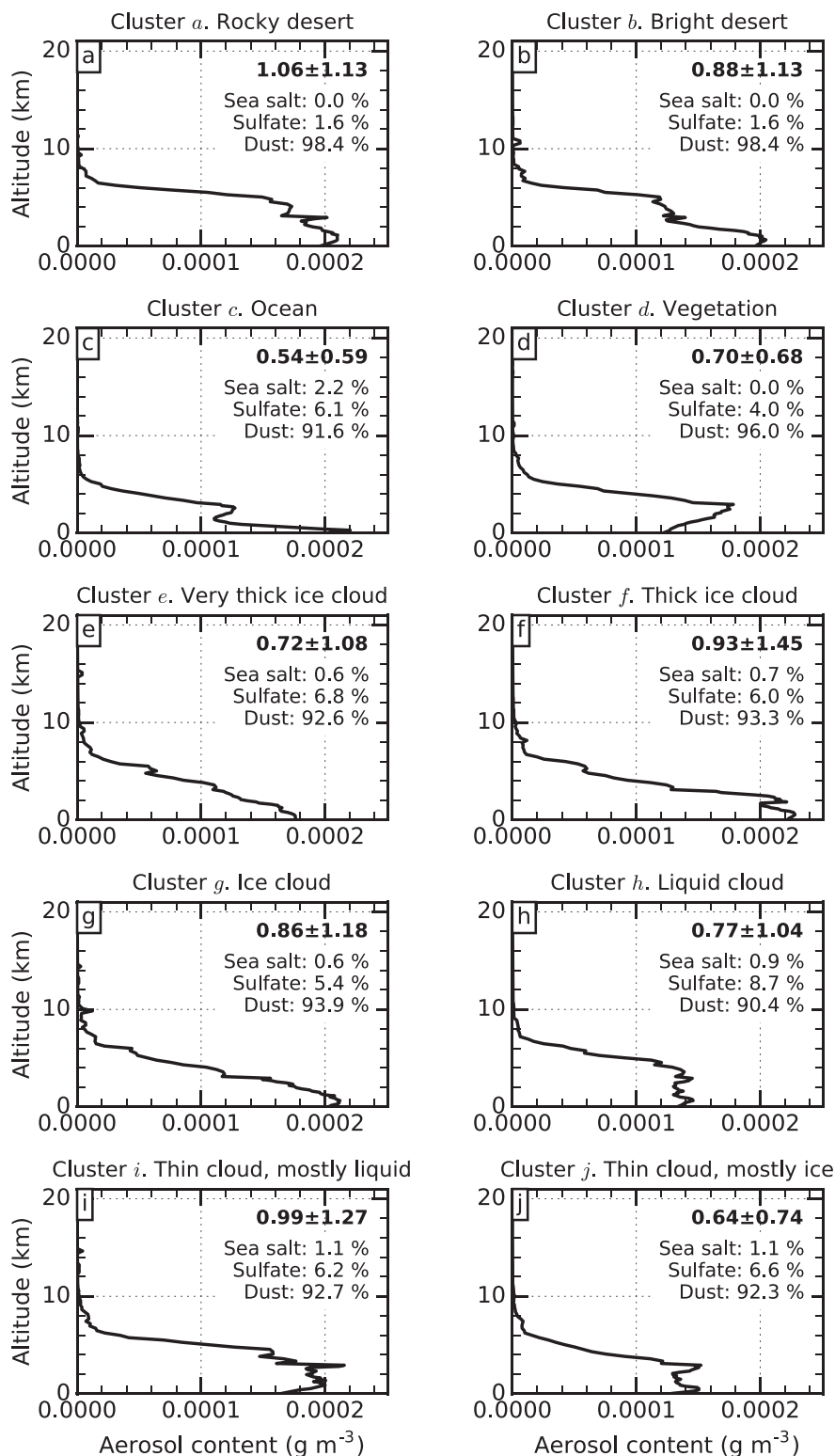
FIG. 6. The mean vertical profile of aerosol used in computed SCIAMACHY-like reflectance spectra belonging to each of the 10 clusters presented in Fig. 1. The vertically integrated aerosol for the mean aerosol vertical profile of each cluster is displayed on each plot, along with ± 1 standard deviation of individual vertically integrated aerosol contents (g m^{-2}). Sea salt, sulfate, and dust are included, and their mean relative percentage, by mass, is also displayed on each plot.

FIG. 7. The mean spectral SWCRE for computed SCIAMACHY-like reflectance spectra belonging to each of the six cloud clusters presented in Fig. 1b. To the right of the colon in the legend is the mean broadband SWCRE, with ± 1 standard deviation (W m^{-2}). Positive SWCRE represents an increase in reflected solar radiation when clouds are present.

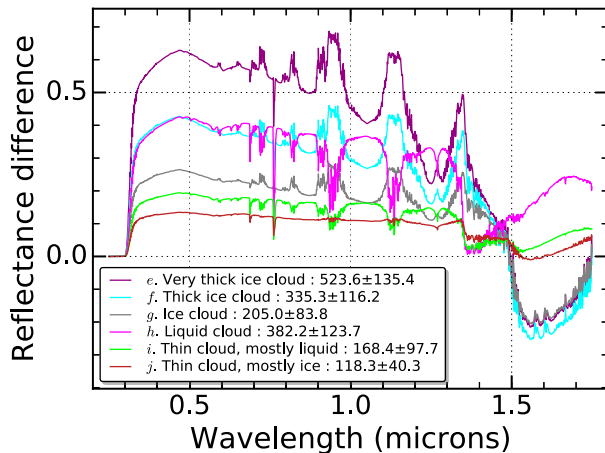clouds are present (most notably clusters h and i). Low-altitude liquid clouds can have appreciable water vapor above (Feldman et al. 2011). Therefore, the radiation experiences substantial water vapor absorption in the presence of clouds, such that the reflectance difference in water vapor absorption bands between cloud-free and cloudy conditions is smaller than that at surrounding wavelengths. The implication is that the reversal in direction of the spectral SWCRE in water vapor absorption bands for different clusters can be related to the vertical positioning of the cloud, rather than variability in water vapor itself.

The mean cloud vertical structures (Fig. 5) and their spectral SWCRE (Fig. 7) together represent an alternative approach to monitoring SWCRE by cloud structure. In the past, a common way to define cloud type has been to use cloud optical thickness and cloud-top height via the International Satellite Cloud Climatology Project (ISCCP) system (Rossow and Schiffer 1999). However, ISCCP cloud types require thresholds to be defined for the cloud-top height boundaries, and it has been shown that the ISCCP cloud types do not always conform to these boundaries (Mace and Wrenn 2013). More recently, with the advent of active remote sensing of clouds from space, clouds have also been classified explicitly by their geometric boundaries using the scheme described by Tselioudis et al. (2013) [henceforth "geometric cloud types"; see Fig. 3 in Hill et al. (2018)]. The geometric cloud types allow for any combination of low- (L), mid- (M), or high-level (H) cloud separated at the ISCCP pressure boundaries of

680 and 440 hPa, with cloud existing either in each layer in isolation or extending across the pressure levels (denoted by an "x" between layers), leading to 12 possible cloud types plus clear sky. Using geometric cloud types, the broadband cloud radiative effects of various cloud vertical structures has recently been revealed (Oreopoulos et al. 2017; Hill et al. 2018). While cloud radiative effects are often closely related to cloud boundaries for longwave radiation, the geometric cloud types have their caveats for shortwave radiation; SWCRE strongly depends on cloud optical depth, but geometrical thickness does not always correlate well with optical depth. For example, we find that some optically thin clouds extend across both ISCCP pressure levels and are classified as HxMxL, which could be misleading since this category is often considered as deep convective clouds. Since the approach put forward here objectively identifies cloud regimes using their spectral radiative signature alone, without the need for predefined cloud boundaries or optical depth thresholds, we consider it to be highly complementary to the existing cloud type definitions for SWCRE investigations.

The spatial domain considered by Hill et al. (2018) falls within the West Africa domain considered here, so we conclude this section by comparing instantaneous broadband SWCRE of the 12 geometric cloud types (Fig. 5a in Hill et al. 2018) to that of our clusters. First, the range in mean broadband SWCRE for our cloud clusters is larger ($\sim$400 W m^{-2}) than for the geometric cloud types ($\sim$330 W m^{-2}). The difference in the range of broadband SWCRE is predominantly because our cloud clusters are defined explicitly by their spectral reflectance. In contrast, clouds with quite different spectral and/or broadband reflectance can belong to the same geometric cloud type as long as the cloud boundaries are similar. Therefore, the geometric cloud type with the lowest mean SWCRE can contain optically thick clouds that will act to increase the mean SWCRE, and the geometric cloud type with the highest mean SWCRE can contain some optically thin clouds that will decrease the mean SWCRE. This leads to the extremes of the SWCRE distribution being not as well captured with the geometric cloud types, hence the smaller overall range in SWCRE.

Second, by assigning each CCCM group to a geometric cloud type using the cloud boundaries, we find that many of the geometric cloud types are widely spread among our clusters (Fig. 8). The four most common geometric cloud types identified by Hill et al. (2018)—1L, 1H, HL, and HxMxL—are each distributed with at least 10% of their frequency among three or four clusters. Surprisingly, the HxMxL type most often falls into cluster h, which has virtually no ice

FIG. 8. The distribution of geometric cloud types and clear sky (CLR) among each of the 10 clusters presented in Fig. 1. Each cloud type is considered in isolation, such that each column adds up to 100%. The geometric cloud type classification allows for any combination of low- (L), mid- (M), or high-level (H) cloud separated at the pressure boundaries of 680 and 440 hPa. An "x" between letters denotes that the cloud extends across the pressure levels.

cloud on average (Fig. 5h). In fact, over 35% of the CCCM groups belonging to the HxMxL type do not contain any ice and generally have much lower total water path than the remaining CCCM groups that do contain ice. Types 1M, ML, HM, and HMxL, which were all found to be less common by Hill et al. (2018), are distributed with at least 10% of their frequency among five or more clusters. Only three geometric cloud types (MxL, HML, and HxMxL) have a frequency of more than 30% in any individual cluster. The implication is that cloud types defined using geometrical boundaries are typically not closely associated with shortwave cloud radiative regimes, particularly for some of the geometric cloud types that occur less frequently.

Finally, we point out that our cluster e, which is associated with very optically thick ice cloud, has a larger mean broadband SWCRE ($523.6 \, \mathrm{W \, m^{-2}}$) than that of any of the 12 geometric cloud types as calculated by Hill et al. (2018). Cluster e appears to select only the optically thickest clouds mostly from the categories of HxMxL, HxM, and 1H (Fig. 8) and therefore arguably provides a better representation of deep convective atmospheric condition from a radiative point of view, as compared with the HxMxL geometric cloud type. The larger SWCRE of our cluster e compared to any of the geometric cloud types emerges despite the generally lower amounts of incoming solar radiation on average for our study; the region in Hill et al. (2018) only extends to 10°N, compared with 30°N here, and they only consider the summer months of June–September, compared

with the entire annual cycle here. This further emphasizes that the cloud regimes identified from spectral radiative signature clustering exhibit an improved variety of SWCRE.

b. Variations with spatial scale

The distinct underlying surface and cloud properties associated with clusters of computed SCIAMACHY-like reflectance spectra present an exciting opportunity to map between spectral observations and physical phenomena. However, the results presented in section 3a are based on cloud profiles and radiative transfer at a 1-km spatial scale. It is unclear whether the cluster centroids from spectra averaged over larger spatial scales change substantially and whether they are still associated with distinct physical properties. We therefore performed the same cluster analysis at two additional spatial scales: the CERES footprint of around 20 km used in the CCCM product, and the SCIAMACHY footprint of around 240 km. These spatial scales are also of interest for modeling; 20 km is comparable to the resolution of global numerical weather prediction models, and 240 km is comparable to the resolution of many climate models.

The results of cluster analysis using SCIAMACHY-like reflectance spectra at 20-km scale are shown in Figs. 9 and 10. Note that the number of spectra is reduced by ∼50% from 90 917 to 39 375 as a result of the spatial averaging. The cluster centroids and mean spectral SWCREs (Fig. 9) are broadly similar to those obtained at 1-km scale, in terms of ice and liquid cloud
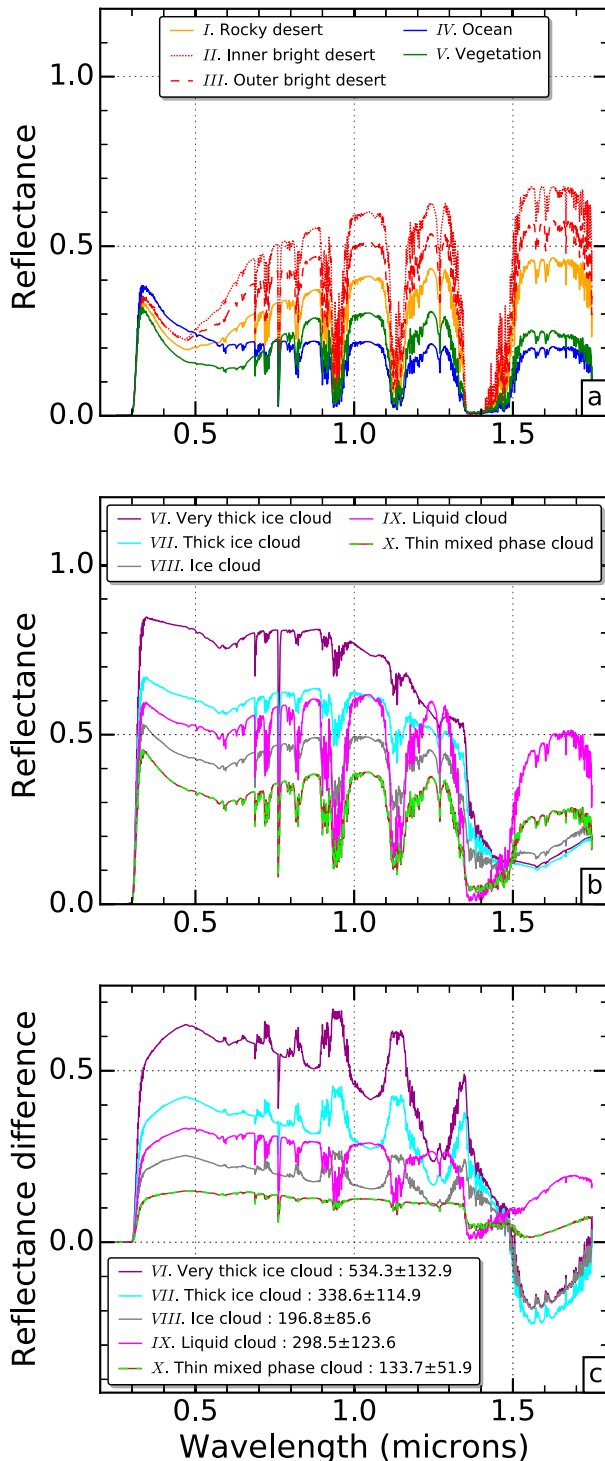
FIG. 9. Cluster centroids of top-of-atmosphere reflectance spectra for (a) surface clusters, (b) cloud clusters, and (c) the mean spectral SWCRE of the cloud clusters. These plots are similar to Figs. 1 and 7, respectively, but instead are based on 39 375 computed SCIAMACHY-like reflectance spectra that have been averaged over a CERES footprint size of around 20 km. To the right of the colon in the legend of (c) is the mean broadband SWCRE for each cluster, with ± 1 standard deviation (W m^{-2}).

absorption features, spectra shape, and overall magnitude of spectral and broadband SWCRE.

More notably, as shown in Fig. 9c, now only five clusters (VI–X) are associated with substantial SWCRE. This indicates that the number of cloud clusters has reduced from six to five, and the number of surface clusters has increased from four to five, compared to the 1-km scale. Closer inspection (Fig. 10) reveals that this change is because clusters i and j (both associated with optically thin cloud) have combined into cluster X, and because cluster b (associated with bright desert surface reflectance) has split into clusters II and III. Physically, the combination of clusters i and j suggests a smaller horizontal cloud scale associated with these clusters. Recall that the vertical positioning of cloud in these clusters is sporadic (Fig. 8), indicating the presence of cloud regimes that are less likely to persist over 20 km when compared to, for example, low-level stratocumulus decks or widespread cirrus. We also found that clusters i and j often occurred next to one another at the 1-km scale, and since their spectral signature is relatively similar, it is not entirely surprising that they combine at the 20-km scale. The splitting of cluster b results from the range in magnitude of desert surface reflectance that changes relatively slowly with spatial scale. While other signatures can be quite strongly diluted with spatial averaging, such as the case described above, the slowly changing magnitude of desert surface reflectance with spatial scale leads to two separate clusters. In other words, the additional surface cluster does not indicate a better surface classification with increased spatial averaging, but reflects the spatial scale at which the underlying atmospheric and surface properties persist. Despite these differences between 20- and 1-km scales, it is still generally the case that the spectral signatures are associated with consistent and distinct physical properties when averaged over 20-km (CERES footprint) scales.

The results of cluster analysis using SCIAMACHY-like reflectance spectra at 240-km scale are shown in Figs. 11 and 12. This further spatial averaging drastically reduced the sample size down to 534. However, by searching for the same number of clusters, spectral signatures at the 240-km resolution exhibit remarkably similar features to those based on 1- and 20-km resolutions. As was the case for the 20-km resolution, the cluster centroids at the 240-km resolution (Figs. 11a,b) still represent ice and liquid cloud absorption features and similar spectra shape. However, the overall magnitude of spectral and broadband SWCRE is lower. A reduction in the highest magnitudes of the SWCRE is not surprising, since the very optically thick clouds controlling these signatures are unlikely to persist over
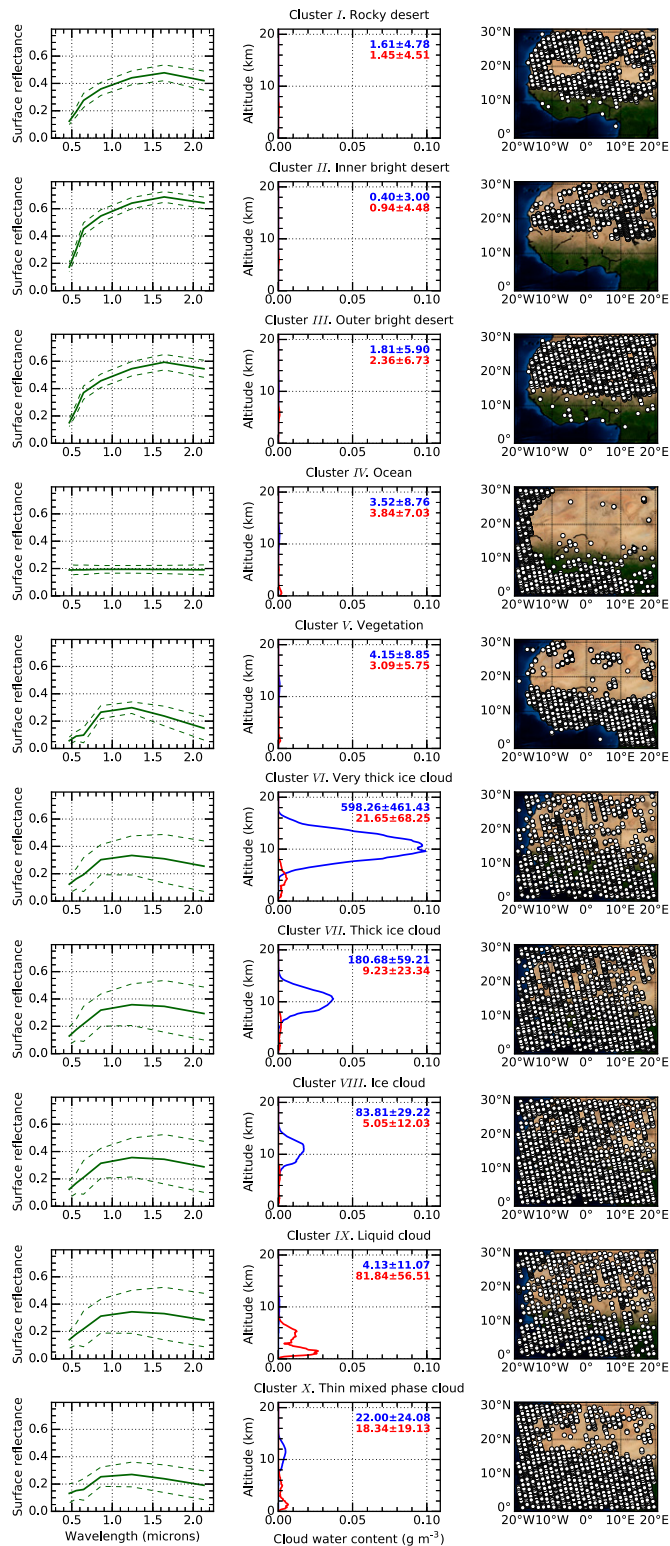
FIG. 10. The mean scene properties used in computed SCIAMACHY-like reflectance spectra that have been averaged over a CERES footprint size of around 20 km and belong to each of the 10 clusters presented in Figs. 9a and 9b. (left) The mean spectral surface reflectance (similar to Fig. 3), (center) the mean vertical profile of cloud water content (similar to Fig. 5), and (right) the location of the spectra (similar to Fig. 4).
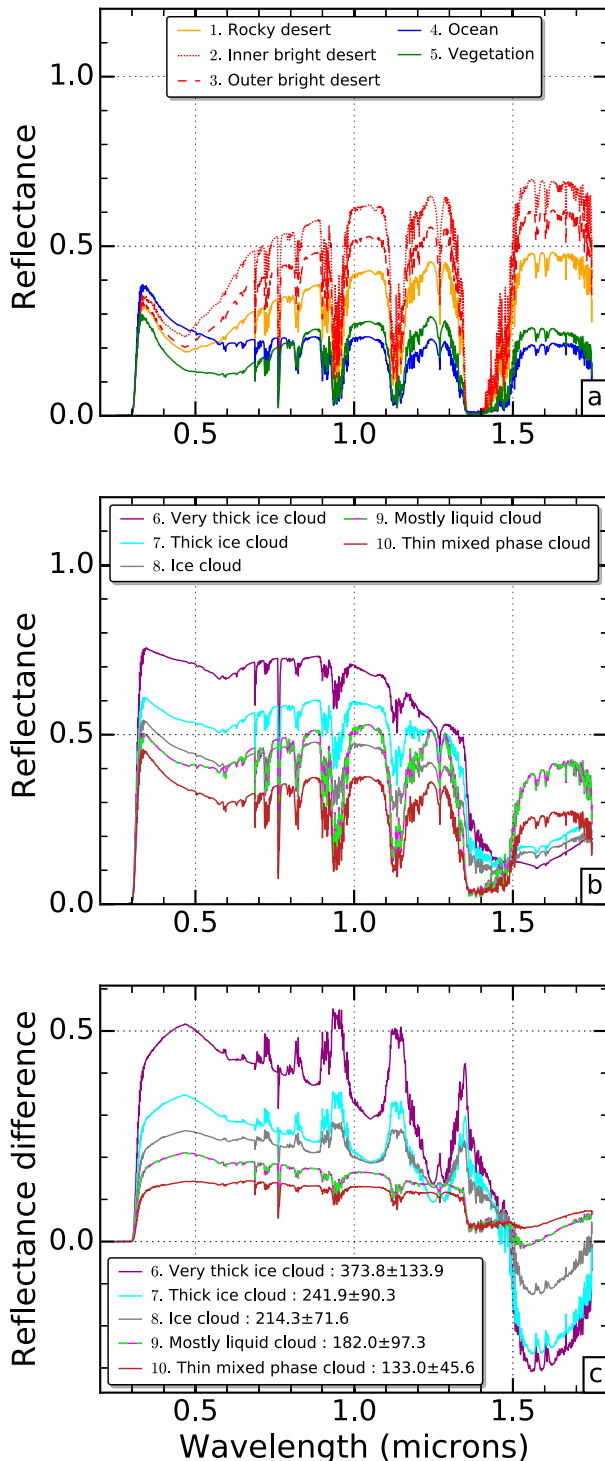
FIG. 11. Cluster centroids of top-of-atmosphere reflectance spectra for (a) surface clusters, (b) cloud clusters, and (c) the mean spectral SWCRE of the cloud clusters. These plots are similar to Figs. 1 and 7, respectively, but instead are based on 534 computed SCIAMACHY-like reflectance spectra that have been averaged over a SCIAMACHY footprint size of around 240 km. To the right of the colon in the legend of (c) is the mean broadband SWCRE for each cluster, with ±1 standard deviation (W m^{-2}).

240 km, but the fact that relatively large SWCRE (i.e., maximum broadband SWCRE of 373.8 W m^{-2}, compared with ~530 W m^{-2} at both 1- and 20-km scales) is still revealed by clustering at this spatial scale is promising.

The split of five surface and five cloud clusters is maintained from 20 to 240 km, but examining the controlling properties (Fig. 12) we find some further subtle changes. At the 240-km scale, it appears that the cloud clusters that were associated with liquid cloud (cluster h) and vertically distributed cloud mostly consisting of liquid water (cluster i) combine into cluster 9. As was the case for the cloud clusters that combined at 20-km scale, cluster h and cluster i commonly occur next to each other, and have similar spectral shape but different magnitude. Since at the 240-km scale there is a reduction in magnitude of SWCRE, the signatures associated with these atmospheric conditions become more similar, providing an explanation for the combination. This gives way for the splitting of the cluster that was associated with bright desert (cluster b) into clusters 2 and 3, similar to the 20-km spatial scale discussed above. It is worth emphasizing that, despite subtle differences, the spectral signatures and controlling properties are remarkably similar between 240- and 1-km resolutions. This demonstrates that, over an undoubtedly mixed scene, spectral signatures from individual dominating properties within that scene can still be detected, which is encouraging for observational studies. These signatures and properties at the 240-km scale are used again in the next section so are summarized in Table 2 for convenience.

c. Assigning observed SCIAMACHY spectra to clusters to examine variability

To assess the extent to which spectral clustering can be used to monitor changes in atmospheric and surface properties from real spectral reflectance observations, SCIAMACHY observations are now assigned to the existing clusters obtained from computed SCIAMACHY-like reflectance spectra at the SCIAMACHY footprint scale (Figs. 11 and 12; Table 2), and the cluster relative frequency of occurrence is examined over time. We choose two time periods to examine cluster relative frequency of occurrence: the annual cycle during 2010, and the West African monsoon seasons of 2003 and 2004. The annual cycle is chosen because progression of the West African monsoon over the region considered here is associated with large seasonal changes in precipitation (Fig. 13a), and 2010 was an active monsoon year (Fig. 14a). Likewise, the West African monsoon seasons of 2003 and 2004 are chosen because these consecutive years exhibited the largest swing in Sahel precipitation, excluding 2010 (Fig. 14a). Consecutive years are used to avoid issues with instrument drift, and excluding 2010 enables us to test
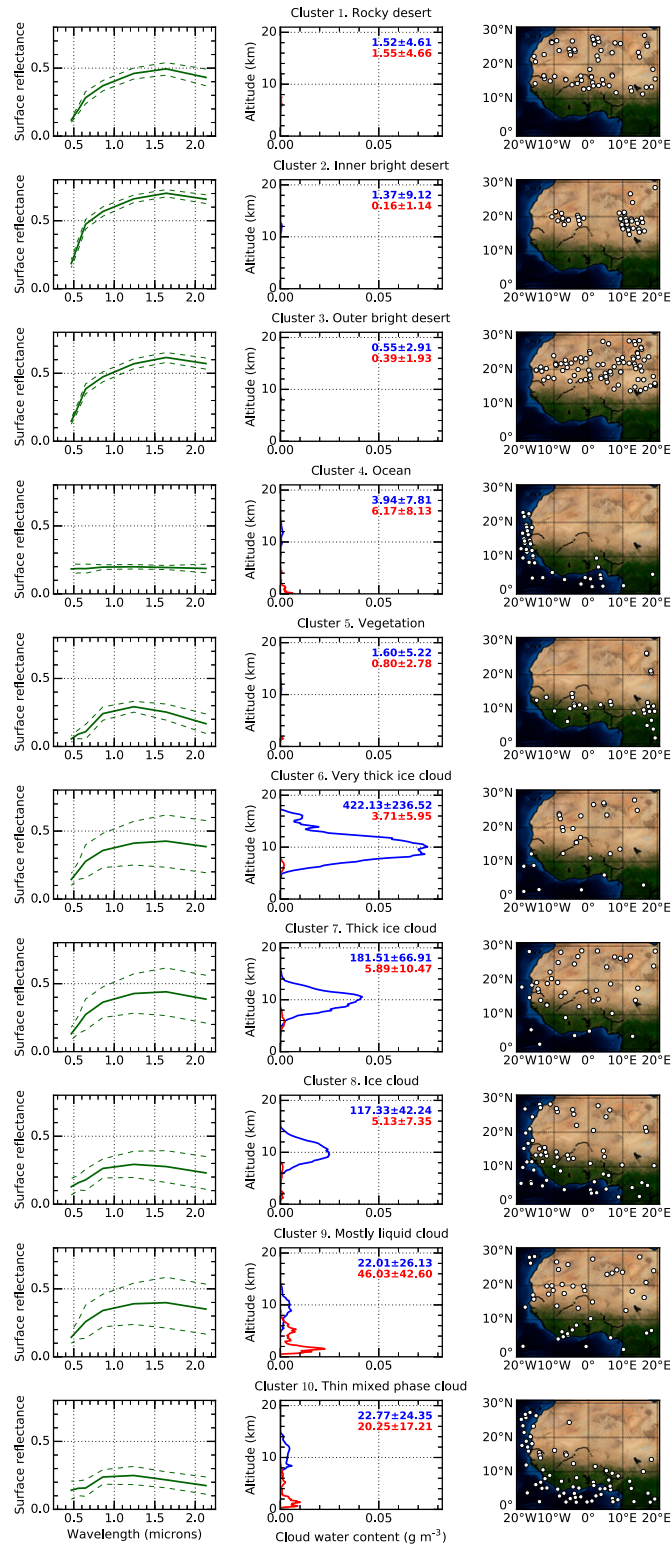
FIG. 12. The mean scene properties used in computed SCIAMACHY-like reflectance spectra that have been averaged over a SCIAMACHY footprint size of around 240 km and belong to each of the 10 clusters presented in Figs. 11a and 11b. (left) The mean spectral surface reflectance (similar to Fig. 3), (center) the mean vertical profile of cloud water content (similar to Fig. 5), and (right) the location of the computed spectra (similar to Fig. 4).

TABLE 2. Summary of the 10 clusters presented in Figs. 11a and 11b and their dominant properties. Based on 534 computed SCIA-MACHY-like reflectance spectra over West Africa in 2010 that have been averaged over a SCIAMACHY footprint size of around 240 km. In the second column, slash (/) and dash (–) symbols indicate splitting and joining relative to the high-resolution clusters, respectively.

Cluster identifier	Relationship with high-resolution cluster	Assigned color	Comment on controlling property	Designated as surface or cloud dominated?	No. of spectra
1	a	Orange	Rocky desert	Surface	64
2	b/	Red dot	*Inner* bright desert (sand dunes)	Surface	87
3	b/	Red dash	*Outer* bright desert (sand dunes)	Surface	55
4	c	Blue	Ocean	Surface	44
5	d	Green	Vegetation	Surface	30
6	e	Purple	Very optically thick ice cloud	Cloud	287
7	f	Cyan	Optically thick ice cloud	Cloud	44
8	g	Gray	Ice cloud	Cloud	63
9	h–i	Magenta and lime dash	Vertically distributed cloud, liquid dominated	Cloud	46
10	j	Brown	Vertically distributed but optically thin cloud over dark surface	Cloud	73

whether the method of assigning observations to clusters leads to useful results outside of the time period that the cluster analysis was performed. Sample size is not a problem for these experiments since over 8000 SCIA-MACHY observations are used for each month during the annual cycle of 2010, and almost 90 000 observations are used to compare 2003 and 2004. Since the precipitation changes over these various time periods only provide an indication of atmospheric activity, this section aims to identify whether these precipitation changes are strongly linked to changes in the surface and cloud regimes defined by reflectance spectra.

The annual cycle of rainfall over West Africa tends to be concentrated in two regions and occur in two different time periods (Fig. 13a). First, intense convection and high rainfall amounts around the Gulf of Guinea (focused just south of 5°N) occur in May–June, driven by sea surface temperature seasonality in the tropical eastern Atlantic (Gu and Adler 2004). Second, an intense rain belt develops over the interior of the West African continent (focused just north of 10°N) persisting from July to September, primarily associated with the intertropical convergence zone (Gu and Adler 2004). These two rainfall peaks are embedded within the larger West African monsoon circulation that is generally considered to be active from June to October (Cornforth 2012). The relative frequency of occurrence of both surface and cloud clusters based on SCIAMACHY observations over West Africa in 2010 (Figs. 13b,c) does not appear to separate the two rainfall peaks, likely because the rainfall peaks are strongly zonal features as opposed to the relative frequencies that are calculated over the entire domain, but it does follow the overall West African monsoon seasonality closely. On average, cloud clusters

have higher relative frequency of occurrence from June to October than any other months during the year. Consequently, the relative frequency of occurrence averaged for surface clusters has a minimum in June–October.

Individual cloud clusters (Fig. 13c) all exhibit West African monsoon seasonality to some extent. However, the change in the average of the cloud clusters is primarily driven by clusters 9 and 10, which are both associated with diverse cloud vertical structures, typical of the West African monsoon (Stein et al. 2011). These two clusters have an annual range in relative frequency of occurrence of 14.5% and 7.9%, respectively. Of the clusters associated with ice cloud (clusters 6, 7, and 8), the largest annual ranges are from clusters 6 and 7, which are associated with the optically thickest ice cloud, also consistent with the key role of convective storms during the monsoon (Marsham et al. 2013).

For the surface clusters (Fig. 13b), the decrease in relative frequency of occurrence during the monsoon season is primarily driven by cluster 5, which has an annual range of 15.5% and is associated with vegetated surfaces. Rather than variations in the surface properties themselves, we expect this large annual range is mostly associated with location. Densely vegetated areas are almost entirely located from 0° to 15°N in the West Africa region, and this is precisely where the monsoon rains progress (Fig. 13a). In other words, the spectra over these surfaces become controlled by cloud signatures during the monsoon season, reducing the relative frequency of vegetation dominated spectra. A similar argument can be made for cluster 4, which is associated with ocean surface signature, since most of the ocean area is in the southern part of the domain. The annual ranges in relative frequency of occurrence are generally
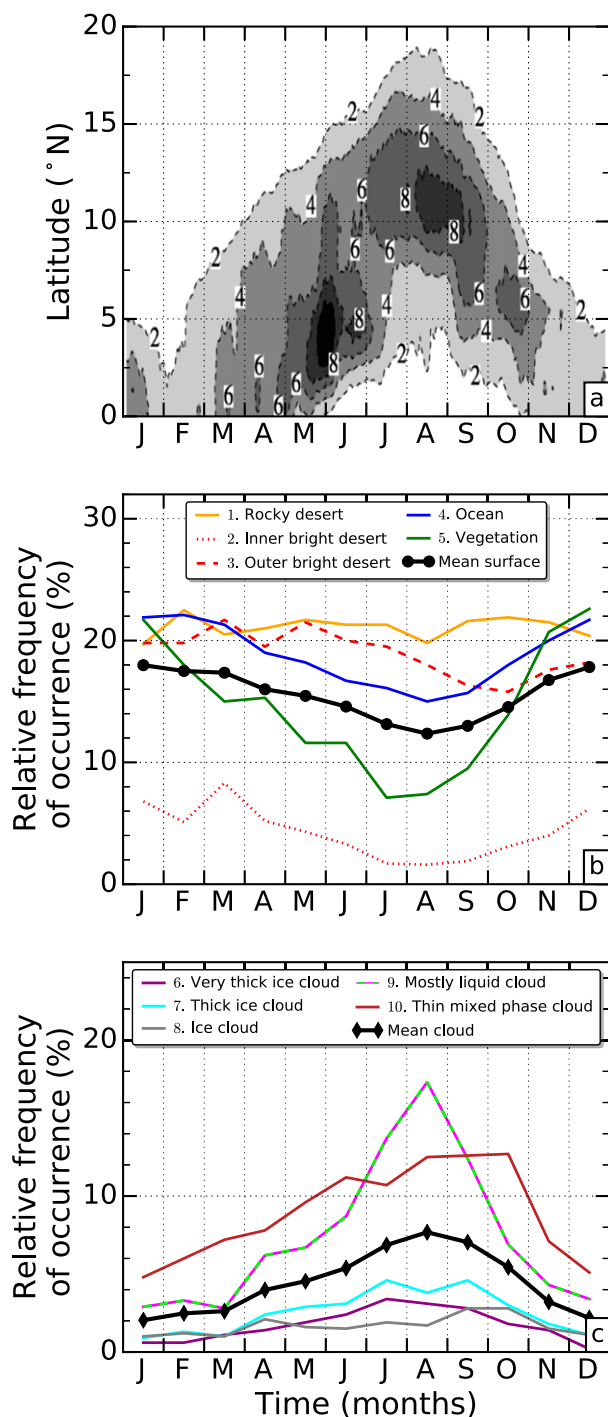
lower for clusters associated with desert surface signature (clusters 1, 2, and 3) since desert surface is, conversely, mostly located in the northern part of the domain where the West African monsoon is of lesser relevance. Despite the pronounced annual cycles of individual clusters, surface clusters remain most frequent on average year-round.

The difference in cluster relative frequency of occurrence between the relatively active monsoon season of 2003 and relatively inactive season of 2004 (Fig. 14a), based on SCIAMACHY observations over West Africa from June to October, appears to capture this interannual variability well (Fig. 14b). Every individual cloud cluster has a higher relative frequency of occurrence in 2003, and every individual surface cluster has a higher relative frequency of occurrence in 2004.

Examining individual clusters, we find that the largest change in relative frequency of occurrence is represented by the same clusters that were most important in the annual cycle for 2010. Cluster 9, associated with a diverse variety of cloud vertical structures, has a relative frequency of occurrence that is 1.8% larger in 2003 than 2004, while other cloud clusters have smaller magnitude changes but consistent sign. Cluster 5, associated with vegetated surface signature, has a relative frequency of occurrence that is 1.7% smaller in 2003 than 2004, while other surface clusters also have smaller magnitude changes but consistent sign. This consistency in cluster relative frequency of occurrence between 2003 and 2004 and throughout 2010 provides evidence that the detected interannual variability is associated with West African monsoon variability, and that assigning observations to clusters can work successfully if applied outside of the time period over which the clustering is performed.

4. Summary and conclusions

To improve understanding of the physical controls on Earth's reflected solar radiation (RSR), over 90 000 top-of-atmosphere solar reflectance spectra have been computed over West Africa in 2010 using atmospheric and surface properties derived from A-Train satellite observations and the spectral characteristics of the SCIAMACHY. By clustering the computed reflectance spectra, 10 clusters, each representing a spectral signature, are extracted and the underlying properties associated with each spectral signature are examined.

The most common extracted spectral signatures are associated with surface reflectance properties. Specifically, signatures related to vegetated, ocean, and desert surfaces are found, as evidenced by the location of the spectra corresponding to each signature and their mean surface spectral reflectance. Similarly, signatures representing distinct cloud

FIG. 13. (a) The annual cycle of West African monsoon rainfall (mm day^{-1}), presented as a 10-day running mean [adapted from Gu and Adler (2004)]. Data are from the Tropical Rainfall Measuring Mission 3B42 product 1998–2003, averaged between 9.5°W and 9.5°E. Monthly cluster relative frequency of occurrence, separated into (b) surface clusters and (c) cloud clusters, for the annual cycle of SCIAMACHY spectral reflectance observations over West Africa in 2010. The clusters used are described in Table 2. The means of the surface and cloud clusters are represented by thick black lines with circle and diamond markers, respectively.
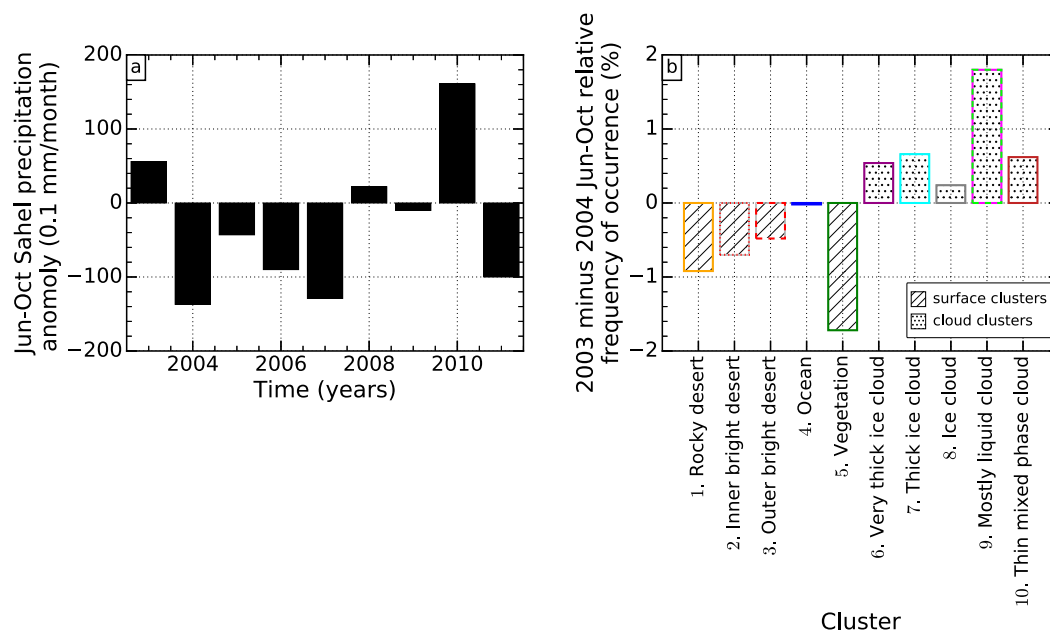
FIG. 14. (a) Sahel precipitation anomalies in June–October for the years coinciding with SCIAMACHY observations [derived from Mitchell (2013)]. Anomalies are relative to 1900–2013, for the region bounded by 20°W–10°E and 10°–20°N. Data are gridded rain gauge anomalies from the National Oceanic and Atmospheric Administration National Climatic Data Center. (b) Difference in cluster relative frequency of occurrence between 2003 and 2004 for SCIAMACHY spectral reflectance observations in June–October over West Africa. The clusters used are described in Table 2, with surface clusters represented by hatching with diagonal lines and cloud clusters by hatching with dots.

regimes are detected, each related to either different optical thicknesses of ice cloud and liquid cloud or different vertical distributions of optically thin cloud. Each of these cloud regimes is distinguished by its spectral SWCRE, which, importantly, can lead to partly compensating influences in equivalent broadband measurements. The mean instantaneous broadband SWCRE associated with the signatures ranges from close to zero for the surface signatures up to more than $500 \, \mathrm{W \, m^{-2}}$ for cloud signatures, which is substantially larger than the ranges presented in other recent studies that have examined the SWCRE of clouds separated by their geometrical boundaries. In fact, clouds with similar geometrical boundaries are found to be widely distributed among the cloud regimes presented here. Since traditional cloud classifications do not appear to be as closely related to SWCRE, the new approach presented in this study, which does not require prior assumptions about cloud location or thickness, is recommended as an alternative way to define cloud types for future SWCRE investigations.

The spectral signatures and their controlling properties found using input from A-Train satellite observations at a spatial scale of 1 km remain remarkably distinct when averaged over 20- and 240-km scales, which are relevant to weather prediction and climate modeling,

current energy budget missions, and available spectral reflectance observations from the SCIAMACHY. This is particularly encouraging for observational studies because the dominating properties controlling spectral variability can still emerge at these spatial scales despite an undoubtedly mixed scene that is not solely populated by its dominating property.

By assigning real SCIAMACHY reflectance observations over West Africa in 2010 to the spectral signatures identified at the 240-km spatial scale, the signatures associated with cloud reflectance are found to be, on average, highest during the active West African monsoon season of June–October. Similarly, signatures associated with surface reflectance are, on average, lowest during this season. Cloud signatures are also found to have a higher relative frequency of occurrence during the active monsoon season of 2003, compared with the inactive monsoon season of 2004. The individual signatures with the largest changes between these years were the same signatures with the largest changes during the annual cycle of 2010, providing further evidence that the change in top-of-atmosphere spectral RSR between the years was associated with variability in the West African monsoon circulation.

The present study establishes a new framework under which there are various opportunities to enhance and

extend the results presented. A similar analysis could be performed globally to determine how the spectral signatures change for a more diverse variety of conditions (e.g., including snow-covered surfaces and polar atmospheres), enabling spectral signatures to be related to global albedo. The radiative transfer code could also be updated to include a wider diversity of aerosol types, in particular to determine the impact of absorbing aerosol on spectral signatures. In addition, further examination of the relationship between spectral reflectance and SWCRE could provide a promising new approach for estimating SWCRE directly from spectral reflectance, but further work would be needed to determine the reliability and uncertainty associated with quantitative SWCRE estimates. Finally, our work here is limited to deriving the instantaneous SWCRE; the application to diurnally resolved, and hence day-averaged, SWCRE would need to await a new generation of satellite configurations.

Overall, the distinct underlying physical properties found to control spectral signatures has revealed the value of the spectral dimension for understanding the controls on the reflected solar radiation by Earth. The utility of the extracted signatures for monitoring intra-annual and interannual variability associated with the West African monsoon has been demonstrated, and presents an alternative route forward for monitoring evolution of the Earth system directly from solar spectral reflectance observations, without the need for simultaneous observations from highly advanced active sensors or retrieval.

REFERENCES

Anderberg, M. R., 1973: *Cluster Analysis for Applications*. Academic Press, 359 pp.

Ansell, C., H. E. Brindley, Y. Pradhan, and R. Saunders, 2014: Mineral dust aerosol net direct radiative effect during GERBILS field campaign period derived from SEVIRI and GERB. *J. Geophys. Res.*, **119**, 4070–4086, https://doi.org/10.1002/2013JD020681.

Barkstrom, B. R., 1984: The Earth Radiation Budget Experiment (ERBE). *Bull. Amer. Meteor. Soc.*, **65**, 1170–1185, https://doi.org/10.1175/1520-0477(1984)065<1170:TERBE>2.0.CO;2.

Bodas-Salcedo, A., P. G. Hill, K. Furtado, K. D. Williams, P. R. Field, J. C. Manners, P. Hyder, and S. Kato, 2016: Large contribution of supercooled liquid clouds to the solar radiation budget of the Southern Ocean. *J. Climate*, **29**, 4213–4228, https://doi.org/10.1175/JCLI-D-15-0564.1.

Brindley, H. E., and J. E. Russell, 2009: An assessment of Saharan dust loading and the corresponding cloud-free longwave direct radiative effect from geostationary satellite observations. *J. Geophys. Res.*, **114**, D23201, https://doi.org/10.1029/2008JD011635.

——, and R. J. Bantges, 2016: The spectral signature of recent climate change. *Curr. Climate Change Rep.*, **2**, 112–126, https://doi.org/10.1007/s40641-016-0039-5.

Cess, R. D., and G. L. Potter, 1987: Exploratory studies of cloud radiative forcing with a general circulation model. *Tellus*, **39A**, 460–473, https://doi.org/10.3402/tellusa.v39i5.11773.

Coddington, O., P. Pilewskie, and T. Vukicevic, 2012: The Shannon information content of hyperspectral shortwave cloud albedo measurements: Quantification and practical applications. *J. Geophys. Res.*, **117**, D04205, https://doi.org/10.1029/2011JD016771.

Cornforth, R., 2012: Overview of the West African monsoon 2011. *Weather*, **67**, 59–65, https://doi.org/10.1002/wea.1896.

Dessler, A. E., 2013: Observations of climate feedbacks over 2000–10 and comparisons to climate models. *J. Climate*, **26**, 333–342, https://doi.org/10.1175/JCLI-D-11-00640.1.

Feldman, D. R., C. A. Algieri, J. R. Ong, and W. D. Collins, 2011: CLARREO shortwave observing system simulation experiments of the twenty-first century: Simulator design and implementation. *J. Geophys. Res.*, **116**, D10107, https://doi.org/10.1029/2010JD015350.

Forster, P. M. F., and J. M. Gregory, 2006: The climate sensitivity and its components diagnosed from Earth Radiation Budget data. *J. Climate*, **19**, 39–52, https://doi.org/10.1175/JCLI3611.1.

Futyan, J. M., J. E. Russell, and J. E. Harries, 2005: Determining cloud forcing by cloud type from geostationary satellite data. *Geophys. Res. Lett.*, **32**, L08807, https://doi.org/10.1029/2004GL022275.

Gottwald, M., and H. Bovensmann, Eds., 2011: *SCIAMACHY—Exploring the Changing Earth's Atmosphere*. Springer, 225 pp., https://doi.org/10.1007/978-90-481-9896-2.

Gu, G., and R. F. Adler, 2004: Seasonal evolution and variability associated with the West African monsoon system. *J. Climate*, **17**, 3364–3377, https://doi.org/10.1175/1520-0442(2004)017<3364:SEAVAW>2.0.CO;2.

Hannak, L., P. Knippertz, A. H. Fink, A. Kniffka, and G. Pante, 2017: Why do global climate models struggle to represent low-level clouds in the West African summer monsoon? *J. Climate*, **30**, 1665–1687, https://doi.org/10.1175/JCLI-D-16-0451.1.

Harries, J. E., H. E. Brindley, and A. J. Geer, 1998: Climate variability and trends from operational satellite spectral data. *Geophys. Res. Lett.*, **25**, 3975–3978, https://doi.org/10.1029/1998GL900056.

——, and Coauthors, 2005: The Geostationary Earth Radiation Budget Project. *Bull. Amer. Meteor. Soc.*, **86**, 945–960, https://doi.org/10.1175/BAMS-86-7-945.

Hartmann, D. L., and P. Ceppi, 2014: Trends in the CERES dataset, 2000–13: The effects of sea ice and jet shifts and comparison to climate models. *J. Climate*, **27**, 2444–2456, https://doi.org/10.1175/JCLI-D-13-00411.1.

Havemann, S., J.-C. Thelen, J. P. Taylor, and R. C. Harlow, 2018: The Havemann–Taylor Fast Radiative Transfer Code (HT-FRTC):

A multipurpose code based on principal components. *J. Quant. Spectrosc. Radiat. Transf.*, **220**, 180–192, https://doi.org/10.1016/j.jqsrt.2018.09.008.

Haywood, J. M., and Coauthors, 2016: The impact of equilibrating hemispheric albedos on tropical performance in the HadGEM2-ES coupled climate model. *Geophys. Res. Lett.*, **43**, 395–403, https://doi.org/10.1002/2015GL066903.

Hill, P. G., R. P. Allan, J. C. Chiu, and T. H. M. Stein, 2016: A multisatellite climatology of clouds, radiation, and precipitation in southern West Africa and comparison to climate models. *J. Geophys. Res. Atmos.*, **121**, 10 857–10 879, https://doi.org/10.1002/2016JD025246.

——, ——, ——, A. Bodas-Salcedo, and P. Knippertz, 2018: Quantifying the contribution of different cloud types to the radiation budget in southern West Africa. *J. Climate*, **31**, 5273–5291, https://doi.org/10.1175/JCLI-D-17-0586.1.

Huang, X., and Y. L. Yung, 2005: Spatial and spectral variability of the outgoing thermal IR spectra from AIRS: A case study of July 2003. *J. Geophys. Res.*, **110**, D12102, https://doi.org/10.1029/2004JD005530.

——, X. Chen, G. L. Potter, L. Oreopoulos, J. N. S. Cole, D. Lee, and N. G. Loeb, 2014: A global climatology of outgoing longwave spectral cloud radiative effect and associated effective cloud properties. *J. Climate*, **27**, 7475–7492, https://doi.org/10.1175/JCLI-D-13-00663.1.

Huang, Y., V. Ramaswamy, X. Huang, Q. Fu, and C. Bardeen, 2007: A strict test in climate modeling with spectrally resolved radiances: GCM simulation versus AIRS observations. *Geophys. Res. Lett.*, **34**, L24707, https://doi.org/10.1029/2007GL031409.

——, S. Leroy, P. J. Gero, J. Dykema, and J. Anderson, 2010: Separation of longwave climate feedbacks from spectral observations. *J. Geophys. Res.*, **115**, D07104, https://doi.org/10.1029/2009JD012766.

Jakob, C., and G. Tselioudis, 2003: Objective identification of cloud regimes in the tropical western Pacific. *Geophys. Res. Lett.*, **30**, 2082, https://doi.org/10.1029/2003GL018367.

Kato, S., S. Sun-Mack, W. F. Miller, F. G. Rose, Y. Chen, P. Minnis, and B. A. Wielicki, 2010: Relationships among cloud occurrence frequency, overlap, and effective thickness derived from CALIPSO and CloudSat merged cloud vertical profiles. *J. Geophys. Res.*, **115**, D00H28, https://doi.org/10.1029/2009JD012277.

——, and Coauthors, 2011: Improvements of top-of-atmosphere and surface irradiance computations with CALIPSO-, CloudSat-, and MODIS-derived cloud and aerosol properties. *J. Geophys. Res.*, **116**, D19209, https://doi.org/10.1029/2011JD016050.

King, N. J., and G. Vaughan, 2012: Using passive remote sensing to retrieve the vertical variation of cloud droplet size in marine stratocumulus: An assessment of information content and the potential for improved retrievals from hyperspectral measurements. *J. Geophys. Res.*, **117**, D15206, https://doi.org/10.1029/2012JD017896.

Knippertz, P., and Coauthors, 2015: The DACCIWA Project: Dynamics–Aerosol–Chemistry–Cloud Interactions in West Africa. *Bull. Amer. Meteor. Soc.*, **96**, 1451–1460, https://doi.org/10.1175/BAMS-D-14-00108.1.

Kokhanovsky, A. A., V. V. Rozanov, W. Lotz, and M. Vountas, 2005: The SCIAMACHY cloud products: Algorithms and examples from ENVISAT. *Adv. Space Res.*, **36**, 789–799, https://doi.org/10.1016/j.asr.2005.03.026.

Kurucz, R., and B. Bell, 1995: Atomic Line Data. CD-ROM No. 23, Cambridge, MA, Smithsonian Astrophysical Observatory, https://www.cfa.harvard.edu/amp/ampdata/kurucz23/sekur.html.

Kyle, H. L., and Coauthors, 1993: The Nimbus Earth Radiation Budget (ERB) Experiment: 1975 to 1992. *Bull. Amer. Meteor. Soc.*, **74**, 815–830, https://doi.org/10.1175/1520-0477(1993)074<0815:TNERBE>2.0.CO;2.

Leroy, S., J. Anderson, J. Dykema, and R. Goody, 2008: Testing climate models using thermal infrared spectra. *J. Climate*, **21**, 1863–1875, https://doi.org/10.1175/2007JCLI2061.1.

Li, J., J. Scinocca, M. Lazare, N. McFarlane, K. von Salzen, and L. Solheim, 2006: Ocean surface albedo and its impact on radiation balance in climate models. *J. Climate*, **19**, 6314–6333, https://doi.org/10.1175/JCLI3973.1.

Loeb, N. G., B. A. Wielicki, F. G. Rose, and D. R. Doelling, 2007: Variability in global top-of-atmosphere shortwave radiation between 2000 and 2005. *Geophys. Res. Lett.*, **34**, L03704, https://doi.org/10.1029/2006GL028196.

Mace, G. G., and F. J. Wrenn, 2013: Evaluation of the hydrometeor layers in the east and west Pacific within ISCCP cloud-top pressure–optical depth bins using merged *CloudSat* and *CALIPSO* data. *J. Climate*, **26**, 9429–9444, https://doi.org/10.1175/JCLI-D-12-00207.1.

Marsham, J. H., N. S. Dixon, L. Garcia-Carreras, G. M. S. Lister, D. J. Parker, P. Knippertz, and C. E. Birch, 2013: The role of moist convection in the West African monsoon system: Insights from continental-scale convection-permitting simulations. *Geophys. Res. Lett.*, **40**, 1843–1849, https://doi.org/10.1002/grl.50347.

Mitchell, T., 2013: Sahel Precipitation Index. Accessed 2018, https://doi.org/10.6069/H5MW2F2Q.

Oreopoulos, L., N. Cho, D. Lee, S. Kato, and G. J. Huffman, 2014: An examination of the nature of global MODIS cloud regimes. *J. Geophys. Res. Atmos.*, **119**, 8362–8383, https://doi.org/10.1002/2013JD021409.

——, ——, and ——, 2017: New insights about cloud vertical structure from CloudSat and CALIPSO observations. *J. Geophys. Res. Atmos.*, **122**, 9280–9300, https://doi.org/10.1002/2017JD026629.

Pilewskie, P., and S. Twomey, 1987: Discrimination of ice from water in clouds by optical remote sensing. *Atmos. Res.*, **21**, 113–122, https://doi.org/10.1016/0169-8095(87)90002-0.

Potter, G. L., J. M. Slingo, J.-J. Morcrette, and L. Corsetti, 1992: A modeling perspective on cloud radiative forcing. *J. Geophys. Res.*, **97**, 20 507–20 518, https://doi.org/10.1029/92JD01909.

Ramanathan, V., 1987: The role of Earth radiation budget studies in climate and general circulation research. *J. Geophys. Res.*, **92**, 4075–4095, https://doi.org/10.1029/JD092iD04p04075.

Roberts, Y. L., P. Pilewskie, and B. C. Kindel, 2011: Evaluating the observed variability in hyperspectral Earth-reflected solar radiance. *J. Geophys. Res.*, **116**, D24119, https://doi.org/10.1029/2011JD016448.

——, ——, D. R. Feldman, and W. D. Collins, 2013: Quantitative comparison of the variability in observed and simulated shortwave reflectance. *Atmos. Chem. Phys.*, **13**, 3133–3147, https://doi.org/10.5194/acp-13-3133-2013.

——, ——, D. R. Feldman, B. C. Kindel, and W. D. Collins, 2014: Temporal variability of observed and simulated hyperspectral reflectance. *J. Geophys. Res.*, **119**, 10 262–10 280, https://doi.org/10.1002/2014JD021566.

Rossow, W. B., and R. A. Schiffer, 1999: Advances in understanding clouds from ISCCP. *Bull. Amer. Meteor. Soc.*, **80**, 2261–2287, https://doi.org/10.1175/1520-0477(1999)080<2261:AIUCFI>2.0.CO;2.

Stein, T. H. M., D. J. Parker, J. Delanoë, N. S. Dixon, R. J. Hogan, P. Knippertz, R. I. Maidment, and J. H. Marsham, 2011: The vertical cloud structure of the West African monsoon: A 4 year

climatology using CloudSat and CALIPSO. *J. Geophys. Res.*, **116**, D22205, https://doi.org/10.1029/2011JD016029.

Stephens, G. L., D. O'Brien, P. J. Webster, P. Pilewski, S. Kato, and J. Li, 2015: The albedo of Earth. *Rev. Geophys.*, **53**, 141–163, https://doi.org/10.1002/2014RG000449.

——, M. Z. Hakuba, M. Hawcroft, J. M. Haywood, A. Behrangi, J. E. Kay, and P. J. Webster, 2016: The curious nature of the hemispheric symmetry of the Earth's water and energy balances. *Curr. Climate Change Rep.*, **2**, 135–147, https://doi.org/10.1007/s40641-016-0043-9.

Stockli, R., E. Vermote, N. Z. Saleous, R. Simmon, and D. Herring, 2005: The Blue Marble Next Generation—A true color earth dataset including seasonal dynamics from MODIS. Accessed 2018, https://www.researchgate.net/publication/252137621_The_Blue_Marble_Next_Generation_-_A_true_color_earth_dataset_including_seasonal_dynamics_from_MODIS.

Tett, S. F. B., M. J. Mineter, C. Cartis, D. J. Rowlands, and P. Liu, 2013a: Can top-of-atmosphere radiation measurements constrain climate predictions? Part I: Tuning. *J. Climate*, **26**, 9348–9366, https://doi.org/10.1175/JCLI-D-12-00595.1.

——, D. J. Rowlands, M. J. Mineter, and C. Cartis, 2013b: Can top-of-atmosphere radiation measurements constrain climate predictions? Part II: Climate sensitivity. *J. Climate*, **26**, 9367–9383, https://doi.org/10.1175/JCLI-D-12-00596.1.

Tselioudis, G., W. Rossow, Y. Zhang, and D. Konsta, 2013: Global weather states and their properties from passive and active satellite cloud retrievals. *J. Climate*, **26**, 7734–7746, https://doi.org/10.1175/JCLI-D-13-00024.1.

Voigt, A., B. Stevens, J. Bader, and T. Mauritsen, 2013: The observed hemispheric symmetry in reflected shortwave irradiance. *J. Climate*, **26**, 468–477, https://doi.org/10.1175/JCLI-D-12-00132.1.

——, ——, ——, and ——, 2014: Compensation of hemispheric albedo asymmetries by shifts of the ITCZ and tropical clouds. *J. Climate*, **27**, 1029–1045, https://doi.org/10.1175/JCLI-D-13-00205.1.

Vonder Haar, T. H., and V. E. Suomi, 1971: Measurements of the Earth's radiation budget from satellites during a five-year period. Part I: Extended time and space means. *J. Atmos. Sci.*, **28**, 305–314, https://doi.org/10.1175/1520-0469(1971)028<0305:MOTERB>2.0.CO;2.

von Hoyningen-Huene, W., and Coauthors, 2007: Validation of SCIAMACHY top-of-atmosphere reflectance for aerosol remote sensing using MERIS L1 data. *Atmos. Chem. Phys.*, **7**, 97–106, https://doi.org/10.5194/acp-7-97-2007.

Wielicki, B. A., B. R. Barkstrom, E. F. Harrison, R. B. Lee, G. Louis Smith, and J. E. Cooper, 1996: Clouds and the Earth's Radiant Energy System (CERES): An Earth observing system experiment. *Bull. Amer. Meteor. Soc.*, **77**, 853–868, https://doi.org/10.1175/1520-0477(1996)077<0853:CATERE>2.0.CO;2.

Williams, K. D., and G. Tselioudis, 2007: GCM intercomparison of global cloud regimes: Present-day evaluation and climate change response. *Climate Dyn.*, **29**, 231–250, https://doi.org/10.1007/s00382-007-0232-2.

——, and M. J. Webb, 2009: A quantitative performance assessment of cloud regimes in climate models. *Climate Dyn.*, **33**, 141–157, https://doi.org/10.1007/s00382-008-0443-1.

Young, M., 2015: Improved rainfall monitoring for Africa. Ph.D. thesis, University of Reading, 153 pp.

Zhang, Y., S. Klein, G. G. Mace, and J. Boyle, 2007: Cluster analysis of tropical clouds using CloudSat data. *Geophys. Res. Lett.*, **34**, L12813, https://doi.org/10.1029/2007GL029336.